Mineralogical Magazine (2021), **85**, 568–587
doi:10.1180/mgm.2021.6

CAMBRIDGE UNIVERSITY PRESS

Article – Gregory Yu. Ivanyuk memorial issue

Composition and genesis of albitite-hosted antecrystic pyrochlore from the Sevattur carbonatite complex, India

Monojit Dey[1], Roger H. Mitchell[2], Sourav Bhattacharjee[1], Aniket Chakrabarty[1]*, Supriyo Pal[3], Supratim Pal[4] and Amit Kumar Sen[3]

[1]Department of Earth and Climate Science, Indian Institute of Science Education and Research Tirupati, Rami Reddy Nagar, Karakambadi Road, Mangalam, Andhra Pradesh 517507, India; [2]Department of Geology, Lakehead University, Thunder Bay, Ontario, Canada P7B 5E1; [3]Department of Earth Sciences, Indian Institute of Technology Roorkee, Roorkee, Uttarakhand 247667, India; and [4]Department of Geology, Durgapur Government College, Durgapur, West Bengal 713214, India

Abstract

The Neoproterozoic Sevattur complex is composed essentially of calcite and dolomite carbonatites together with pyroxenites and diverse syenites. This work reports the compositions and paragenesis of different pyrochlore generations hosted by albitite veins in this complex. The pyrochlore are distinctive, being exceptionally rich in uranium (26 to 36 wt.% UO_2). Five types of pyrochlore (Pcl-I to Pcl-V) are recognised on the basis of composition and texture. With the exception of Pcl-V, the majority of the pyrochlore (Pcl-II to Pcl-IV) are surrounded by a thick orbicular mantle of Ba-rich potassium feldspar. This mantle around Pcl-V is partially-broken. Pcl-I is restricted to the cores of crystals, and associated with Pcl-II and -III and is relatively rich in Nb (0.53–0.62 apfu) together with more *A*-site vacancies (0.37–0.71 apfu) compared to Pcl-II to Pcl-IV. Other pyrochlore (Pcl-II to Pcl-IV) are characterised by elevated Ca and Ti compared to Pcl-I, which are related to the ($3Nb^{5+} + Na^{+} \rightarrow 3Ti^{4+} + U^{4+}$) and ($2Nb^{5+} \rightarrow 2Ti^{4+} + Ca^{2+}$) substitutions, respectively. These substitutions represent replacement of Pcl-II to Pcl-IV. Alteration and Ba-enrichment in all the pyrochlore are marked by interaction with an externally-derived Ba-rich hydrothermal fluid following the ($2Nb^{5+} \rightarrow 2Ti^{4+} + Ba^{2+}$) substitution. This substitution, coupled with extensive metamictisation leads to the formation of Ba-rich (15.9–16.3 wt.% BaO) patchy-zoned Pcl-V. The orbicular mantles around Pcl-I to Pcl-IV have prevented extensive metamictisation and extensive secondary alteration compared to Pcl-V, where mantling is partially disrupted. The compositional and textural variation suggests that Pcl-II to Pcl-IV form by nucleation on Pcl-I, and are transported subsequently as antecrysts in the host albitite.

Keywords: U-rich pyrochlore, orbicular mantle, albitite, Sevattur carbonatite

(Received 21 August 2020; accepted 20 January 2021; Accepted Manuscript published online: 28 January 2021; Associate Editor: Anton R. Chakhmouradian)

Introduction

Niobium (Nb), tantalum (Ta), zirconium (Zr), hafnium (Hf) and uranium (U) are referred to in geochemistry as high-field-strength elements (HFSE). They show similar geochemical behaviour and have high ratios of valence to ionic radius. Niobium is insoluble in most geological fluids and commonly forms complexes with strong ligands such as O^{2-}, OH^{-} and F^{-}. Consequently, naturally occurring Nb-bearing oxide minerals are more common than niobosilicates (Linnen *et al.*, 2014; Mitchell, 2015). Currently, the Brazilian deposits of Araxá and Catalão-II together with St. Honoré, Canada, account for ~99% of the worldwide niobium production (Chakhmouradian *et al.*, 2015; Giovannini *et al.*, 2020; Mitchell *et al.*, 2020). Experimental studies have shown that Nb solubility increases in alkaline silicate melts (Linnen and Cuney, 2005) and attains very high solubilities in carbonatitic melts (Mitchell and Kjarsgaard, 2002, 2004; Mitchell, 2015). Consequently, Nb-deposits are hosted by carbonatites, alkaline-to-peralkaline granites and syenites, and peraluminous granites and pegmatites (Linen *et al.*, 2014; Mackay and Simandl, 2014; Mitchell, 2015; Verplanck *et al.*, 2016; Dostal *et al.*, 2016).

The primary sources of Nb in carbonatite-hosted deposits are pyrochlore-group minerals, which are cubic Nb–Ta–Ti oxides with the ideal structural formula $A_2B_2O_6Z$ (Hogarth *et al.*, 2000; Atencio *et al.*, 2010; Mitchell *et al.*, 2020). The crystal structure of the pyrochlore-group minerals is flexible and accommodates diverse cations in the eightfold-coordinated *A* [Na^{+}, Ca^{2+}, Mn^{2+}, Ba^{2+}, Fe^{2+}, Sr^{2+}, Sn^{2+}, Pb^{2+}, Sb^{3+}, Y^{3+}, REE^{3+} (rare earth elements), Th^{4+}, U^{4+}, vacancies (□), H_2O], and octahedrally-coordinated *B* (Nb^{5+}, Ta^{5+}, Sb^{5+}, W^{6+}, Ti^{4+}, Si^{4+}, Zr^{4+}, Hf^{4+}, Sn^{4+}, Fe^{3+}, Al^{3+}, V^{5+}) sites, respectively. In contrast, the *Z* site is occupied mainly by F^{-}, OH^{-}, O^{2-}, □, H_2O or very large monovalent cations (>>1.0 Å), such as K^{+}, Rb^{+} or Cs^{+} (Atencio *et al.*, 2010). In carbonatites, pyrochlore are non-stoichiometric and typical compositions can be represented as $[(Ca,Na,U^{4+},Th,REE^{3+},Ba,Sr)_{2-x}(Nb,Ti,Ta,Zr,Fe^{3+})_2O_6(OH,F)_{1-y}\cdot zH_2O]$ where, in the more common members of the group, cations are listed approximately in their order of decreasing importance. Primary

*Author for correspondence: Aniket Chakrabarty, Email: aniket_chakrabarty@rediffmail.com; aniketc@iisertirupati.ac.in

This paper is part of a thematic set 'Alkaline Rocks' in memory of Dr Gregory Yu. Ivanyuk

Cite this article: Dey M., Mitchell R.H., Bhattacharjee S., Chakrabarty A., Pal S., Pal S. and Sen A.K. (2021) Composition and genesis of albitite-hosted antecrystic pyrochlore from the Sevattur carbonatite complex, India. *Mineralogical Magazine* **85**, 568–587. https://doi.org/10.1180/mgm.2021.6

(magmatic) pyrochlore are enriched in Ca, Na, Nb, Ta and F (Melgarejo *et al.*, 2012; Chakhmouradian *et al.*, 2015; Mitchell, 2015; Walter *et al.*, 2018; Mitchell *et al.*, 2020). In contrast, late-stage pyrochlore are formed by hydrothermal and supergene alteration of the primary pyrochlore through a series of complex substitutions involving *A*- and *B*-site cations. These are usually hydrated, cation- and anion-deficient minerals. The most common late-stage pyrochlore composition is $[(Ba,Sr,REE^{3+},Pb,Ca,U^{4+},Th)_{\Sigma<<2}(Nb,Ti,Ta,Zr,Fe^{3+},Si)_2(O,OH)_6(OH,F)_{\Sigma<<1}\cdot zH_2O]$ (Lumpkin and Ewing, 1995; Bonazzi *et al.*, 2006; Chakhmouradian *et al.*, 2015; Mitchell, 2015). These compositional variabilities make pyrochlore-group minerals an excellent indicator for evaluating the magmatic, hydrothermal or supergene processes involved in the formation of the carbonatites and associated alkaline rocks (Zurevinski and Mitchell, 2004; Mitchell, 2015; Walter *et al.*, 2018; Giovannini *et al.*, 2020).

Twenty-six major carbonatite complexes have been reported from the Indian subcontinent (Krishnamurthy, 2019; Paul *et al.*, 2020; Randive and Meshram, 2020). Among these, the Cretaceous Amba Dongar, Gujarat; the Tertiary Sarnu-Dandali complex, Rajasthan and the Neoproterozoic Sevattur (also known as Sevathur) alkaline-carbonatite complex are known for the commercial mining of fluorite, REE and vermiculite, respectively (Viladkar and Subramanian, 1995; Palmer and Williams-Jones, 1996; Bhushan and Kumar, 2013; Bhushan, 2015). The Sevattur complex consists of several generations of calcite-, dolomite- and silico-carbonatites together with pyroxenites, syenites and fenites (Udas and Krishnamurthy, 1970; Viladkar and Subramanian, 1995; Schleicher *et al.*, 1998; Ackerman *et al.*, 2017; Schleicher, 2019). Previous studies have demonstrated that this complex contains significant amounts of U–Ba-rich pyrochlore, hosted mainly by dolomite carbonatite and the weathered soil horizon (Borodin *et al.*, 1971; Udas and Krishnamurthy, 1970; Viladkar and Bismayer, 2014). This work describes new occurrences and presents compositional data for albitite-hosted U-rich pyrochlore from the Sevattur carbonatite complex. We also provide new insights into the genesis of the different pyrochlore generations during the successive stages of their compositional evolution.

Regional geology and albitite petrography

The Sevattur complex (12°25′12″N, 78°31′12″E) is an arcuate-shaped intrusion (1600 m×300 m), composed of different generations of carbonatite, pyroxenite, varieties of syenite and vermiculite-bearing mica pyroxenite (hereafter mica pyroxenite) (Fig. 1a), together with fenites (Udas and Krishnamurthy, 1970; Borodin *et al.*, 1971; Krishnamurthy, 1977; Subramanian *et al.*, 1978; Viladkar and Subramanian, 1995; Schleicher *et al.*, 1998; Ackerman *et al.*, 2017; Schleicher, 2019). The central part of the complex is composed mainly of calcite carbonatite, dolomite carbonatite and a silicate-rich carbonatite (silicocarbonatite), with minor occurrences of ankerite carbonatite (Fig. 1a) (Viladkar and Subramanian, 1995; Viladkar and Bismayer, 2014; Ackerman *et al.*, 2017). The mineralogically distinct carbonatites were emplaced during multiple phases of magmatism, as evidenced by the presence of different apatite and calcite generations within the calcite and dolomite carbonatites (Schleicher, 2019). On the basis of our field observations, the silicate-rich carbonatites occur as two types: a banded variety with alternate bands of silicate and carbonate; and a blue-coloured variety characterised by abundant blue amphibole (magnesio-riebeckite, ferri-winchite) and aegirine. This unit is termed the 'blue carbonatite' (Fig. 1b,c). The origin of these silicate-rich carbonatites remains a matter of debate due to their similarity with the fenites. However, similar richterite-, ferri-winchite-, magnesio-arfvedsonite-, magnesio-riebeckite-, and aegirine-rich blue dolomite carbonatites could be a product of magmatic differentiation as exemplified by the Cargill (Canada) (Pressacco, 2001; Rukhlov and Bell, 2010), Fen (Norway) (Andersen, 1986), and Blue River (Canada), carbonatites (Chudy 2013; Mitchell *et al.*, 2017). Note that Elliot *et al.*, (2018) have also suggested that such assemblages might be a result of late-stage fenitisation during multiple stages of carbonatitic magmatism. The central carbonatite units are surrounded by diverse syenites, although their relationship to the carbonatites is unclear (Fig. 1a). The age of the Sevattur carbonatite been determined as 801±18 Ma (Schleicher *et al.*, 1997). However, precise lithology-specific age data are not available.

The present investigation was undertaken on freshly-exposed albitite veins which cross-cut the silicate-rich carbonatite (blue carbonatite) in the western and south-eastern (active pit) parts of the vermiculite mine. These veins are 2–12 cm in thickness and do not have surficial exposures (Fig. 1b,c). These veins mainly intrude the blue carbonatite and have rarely invaded the mica pyroxenite.

Macroscopically, the albitites are medium-to-coarse grained and composed primarily of pure albite (>95 vol.%), together with calcite, magnesio-riebeckite, ferri-winchite, pyrochlore, baryte, phlogopite, magnetite, pyrite and thorite, in order of decreasing modal abundance (Fig. 2). Albite occurs in two distinct textural modes with a bimodal grain-size distribution. The bulk of the matrix is composed of small euhedral-to-subhedral albite crystals (~300 μm) together with large elongated (> 0.5–1 cm) laths of albite macrocrysts (Fig. 2a,b). These large macrocrysts are commonly broken, suggesting post-crystallisation deformational events. The effects of granulation and brecciation are common in the polycrystalline albite matrix (Fig. 2b). The interstices between the smaller albite grains and the fractured albite macrocrysts are filled typically by calcite and phlogopite, demonstrating that these phases post-date the albite matrix and form later in the paragenetic sequence. Discrete clusters of euhedral-to-subhedral blue amphibole (magnesio-riebeckite and ferri-winchite) (100–300 μm) are found within the albite matrix (Fig. 2c).

Most of the pyrochlore are small (<30 μm), and large (>100 μm) grains are rarely present (Fig. 2c,d). The pyrochlore are euhedral-to-subhedral in habit and vary from lemon yellow to orange in colour in plane polarised light (Fig. 2d). The prominent textural feature is the presence of thick (25–30 μm) orbicular haloes of barium-rich potassium feldspar mantling most of the pyrochlore (Fig. 2d). The orbicular mantles are not restricted to the pyrochlore and can also be found around pyrite and magnetite (Fig. 2e,f). To the best of our knowledge, such textural features have not been previously reported. Discrete grains of Ba-rich potassium feldspar are rare and when present they are partially-replaced by albite (Fig. 2g). Baryte is restricted mainly to these mantles and discrete baryte grains are scarce (Fig. 2g). Sporadic zircon grains (>500 μm) are also present and contain numerous inclusions of thorite (Fig. 2h).

Experimental methods

The compositions of silicates and pyrochlore were analysed in polished thin sections using a CAMECA SX100 electron microprobe (EMP) at the Institute Instrumentation Centre (IIC), Indian Institute of Technology Roorkee. Polished thin sections

https://doi.org/10.1180/mgm.2021.6 Published online by Cambridge University Press

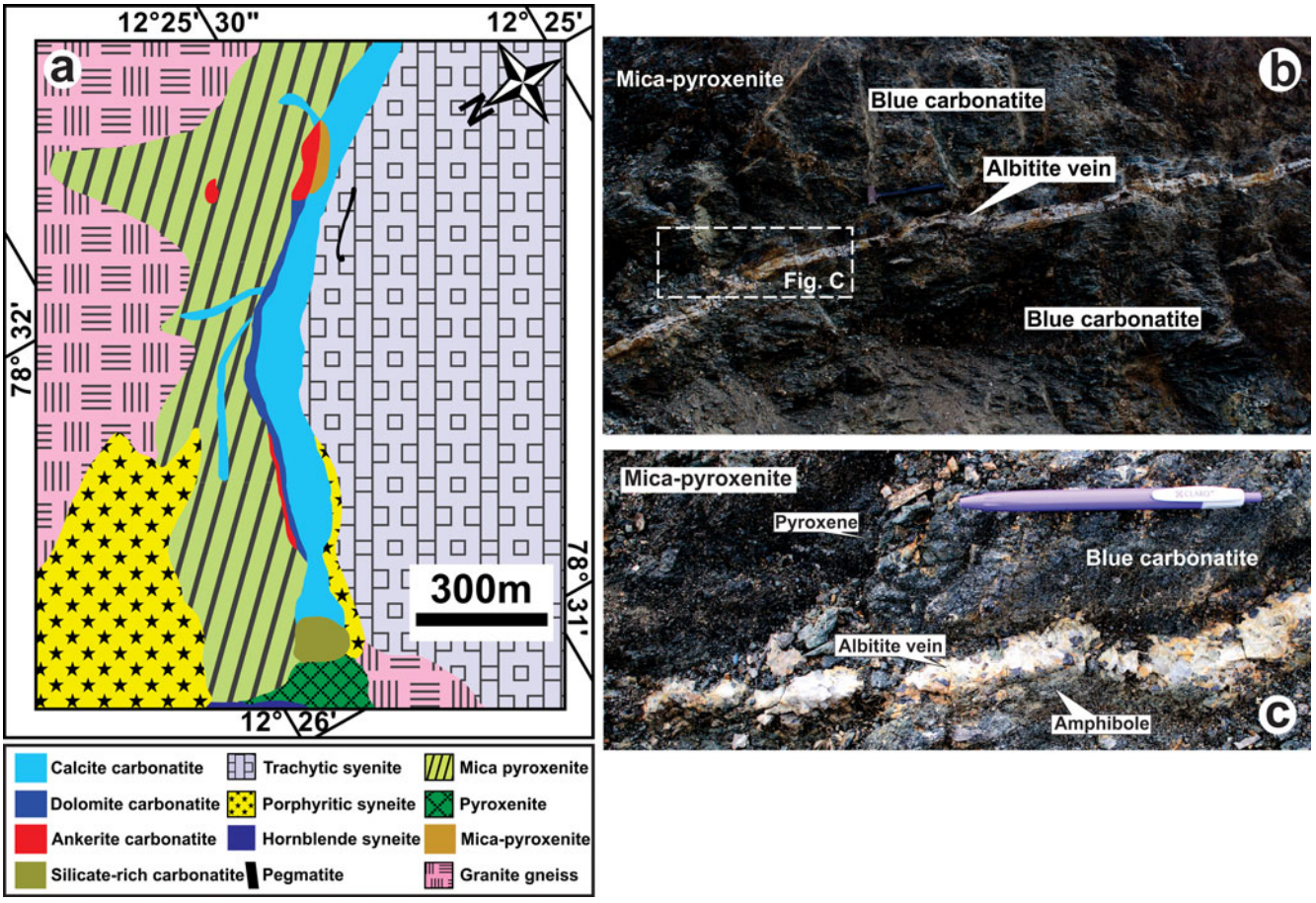

Fig. 1. (a) Regional geological map of a part of the Sevattur carbonatite complex illustrating the disposition of different lithological units (modified after Ramasamy *et al.*, 2001). (b–c) Field photograph of the albitite vein cross-cutting the silicate-rich blue carbonatite unit. Note that the spatially-associated vermiculite-bearing mica pyroxenite is located at the north-western part of the albitite vein (b). Pen used as scale in (c) is 15 cm long.

were examined by optical microscopy to identify the potential target areas for analysis before EMP data collection. Selection of analytical sites was guided by back-scattered electron (BSE) imagery. The instrument, operated in wavelength dispersive (WD) modes is equipped with four WD spectrometers and one energy dispersive (ED) spectrometer. Analytical conditions for most of the silicates were: 15 kV accelerating voltage; 15 nA beam current; and 10 µm beam diameter. For pyrochlore, a focused beam diameter between 1 and 5 µm was used because of the small grain size with a beam current of 10 nA and an acceleration voltage of 20 kV. For calibration, the following standards were used: jadeite (Si*K*α, Na*K*α, Al*K*α); diopside (Ca*K*α); periclase (Mg*K*α); zircon (Zr*L*α); rutile (Ti*K*α); Nb metal (Nb*L*α); Ta metal (Ta*M*α); Al_2O_3 (Al*K*α); rhodonite (Mn*K*α); galena (Pb*K*α); baryte (Ba*L*α); celestine (Sr*L*α); hematite (Fe*K*α); orthoclase (K*K*α); fluorite (F*K*α); and pure synthetic REE phosphates (REE*L*α for La, Ce, Yb, Lu; REE*L*β for the remaining REEs); YPO_4 (Y*L*α); UO_2 (U*M*β); and ThO_2 (Th*M*α). Special attention was given to ensure that line overlaps were corrected adequately and that background interferences were avoided. Empirically determined correction factors were applied to the following line overlaps: Th→U and Ce→Gd (Pršek *et al.*, 2010). Counting times were 15–30 s on peak, and half of that on each baseline for most of the elements, except for F where peak counting time was kept at 60 s. PAP matrix corrections were used (Pouchou and Pichoir, 1991). In all analyses, Na and K were analysed during the first WDS cycle to minimise any element migration arising from beam damage of the sample. Analytical precision on the basis of replicate analyses of standards, suggests standard deviations <0.5% for major and <0.1% for minor elements.

Some replicate and additional analyses of all the major silicate phases and pyrochlore were undertaken at Lakehead University (Canada) by quantitative energy dispersive X-ray spectrometry (EDS) using a Hitachi FE-SU70 scanning electron microscope equipped with *AZtec* software (Oxford Instruments). Quantitative composition data for all minerals were acquired by this instrument as described in Mitchell and Smith (2017) using an accelerating voltage of 20 kV and a beam current of 0.3 nA. Analytical standards used were: apatite (P, Ca); $SrTiO_3$ (Sr, Ti); $ThNb_4O_{12}$ (Th, Nb); Mn-rich fayalite (Mn, Fe, Mg and Si); jadeite (Na, Al); benitoite (Ba, Ti); individual rare-earth orthophosphate glasses; and Ta and U metals. The X-ray spectra for all the major elements were collected for 120 s and for F a CaF_2 standard was used with a collection time of 250 s. No peak overlaps were observed by O*K*α or Fe*K*α with F*K*α. The small beam (1 µm) diameter and low beam currents (0.3 nA) were employed for accurate and reproducible analysis of compositionally different small areas of pyrochlore. All feldspars were analysed with a beam rastered over areas ranging from 100 to 1000 μm^2 to minimise Na volatilisation.

https://doi.org/10.1180/mgm.2021.6 Published online by Cambridge University Press

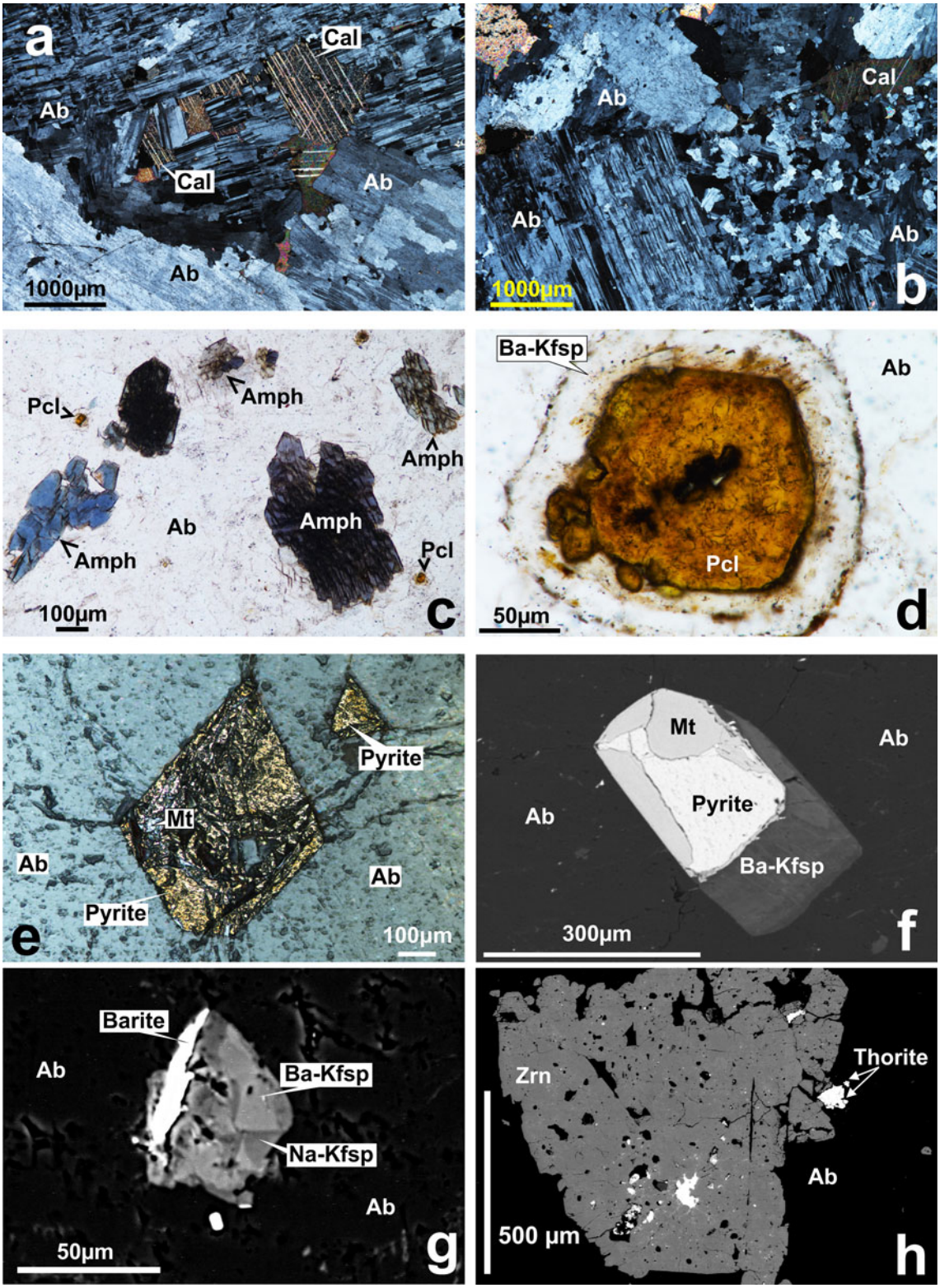

Fig. 2. Transmitted light (a–d), reflected (e), and back-scattered electron (BSE) images (f–h) illustrating the overall mineralogy of the Sevattur albitite. (a, b) Cross polarised light (XPL) photomicrographs showing the bimodal distribution of albite (Ab) crystals. Note that the medium grained and the macrocrystic albite are occur together. Calcite (Cal) grains are present as fracture filling within the macrocrystic albite. (c) An XPL photomicrograph of blue–green euhedral amphiboles (Amph) set within an albite matrix. A few tiny pyrochlore (Pcl) crystals are also present. (d) An XPL photomicrograph showing a large pyrochlore crystal surrounded by a thick orbicular mantle of Ba-rich potassium feldspar (Ba-Kfsp). (e) Reflected-light image showing euhedral pyrite partially replaced by magnetite along the fractures. (f) BSE image illustrating the partial replacement of the pyrite by magnetite (Mt) with a prominent Ba-rich potassium feldspar mantle. (g) BSE image illustrating the two-stage replacement of potassium feldspars. An initial stage of replacement by albite followed by Ba-rich fluid to form Ba-rich potassium feldspar. Note that an elongated anhedral baryte crystal is attached to the original potassium feldspar. Portions of the potassium feldspar are partially replaced by albite (Na-Kfsp). (h) BSE image of a large subhedral zircon (Zrn) set within an albite matrix. Note that a thorite crystal is associated with the zircon.

https://doi.org/10.1180/mgm.2021.6 Published online by Cambridge University Press

Pyrochlore: parageneses, composition and nomenclature

All of the Nb-oxides in the Sevattur albitites are characterised by Nb>Ti>>Ta (atoms per formula unit: apfu) and are classified as pyrochlore *sensu stricto* (Hogarth, 1977; Atencio *et al.*, 2010), with variable betafite molecular proportions (Fig. 3a). None of the analysed pyrochlore contains greater than 1 wt.% Ta_2O_5, and the microlite molecular proportion never exceeds 1 mol.% (Tables 1, 2). In contrast, all the pyrochlore from the associated dolomite carbonatites are Ta-rich and can contain up to 10.4 wt.% Ta_2O_5 (Viladkar and Bismayer, 2014; authors' unpublished data). In terms of composition, the carbonatite-hosted pyrochlore at Sevattur are far more complex (plumbopyrochlore, uranpyrochlore, bariopyrochlore, Si-rich pyrochlore etc.) than those found in albitite and have distinctive alteration assemblages. The compositional variability of the carbonatite-hosted pyrochlore at Sevattur will be addressed in a separate contribution.

All the Sevattur pyrochlore in the albitite are exceptionally rich in U (26.1–35.7 wt.% UO_2, Tables 1, 2) (Fig. 3b). To date, the most U-rich pyrochlore (>46 wt.% UO_2) has been reported from the Mount Niorkpakhk albitites, Khibina, Kola Peninsula, Russia. Our data suggest that some of the analysed pyrochlore are the second most U-rich pyrochlore (with respect to UO_2 wt.%) known after the Khibina albitites (Chakhmouradian and Mitchell, 2002) (Fig. 3b).

The internal textures of the pyrochlore, such as compositional zoning and alteration, are only evident in BSE images. On the basis of these texture and compositional variations, we have recognised five different types of pyrochlore, namely: Pcl-I to Pcl-V (Figs 4, 5). More than one pyrochlore type can be present within a single grain with specific compositional characteristics or as discrete grains. As noted above, irrespective of type, most of the pyrochlore are surrounded by a thick mantle of Ba-rich potassium feldspar and baryte (Figs 4, 5a). In some pyrochlore (especially pyrochlore-V) this mantle is disrupted, and the pyrochlore exhibits considerable compositional variation compared to other pyrochlore (see Pcl-V below). These different textural and compositional pyrochlore types are described below.

Pyrochlore-I and -II

Bask-scattered electron imagery reveals that the earliest-formed pyrochlore (Pcl-I) occurs exclusively as high-AZ unaltered cores and that the darker low-AZ zones (AZ: average atomic number) are a later-formed pyrochlore-II (Figs 4b, 5b). Discrete Pcl-I grains are absent. Both Pcl-I and -II are devoid of detectable primary zoning, although, Pcl-II is characterised by patchy zoning (Figs 4b, 5b). In a single grain, individual high- and low-AZ zones are separated by numerous intermediate-AZ zones (<50 μm^2) of variable composition. Therefore, no consistent compositional variations were observed between core and rim. However, overall Ti enrichment is evident from the core towards the rim. We chose representative grains with distinctive high-, low- and intermediate-AZ areas for analysis and also to avoid compositional interference.

The most striking compositional characteristic of these pyrochlore is their high UO_2 content (Pcl-I: 31.7–35.7 wt.%; 0.53–0.62 apfu; and Pcl-II: 26.1–34.4 wt.%; 0.42–0.60 apfu) (Table 1). Elemental mapping (Fig. 4) reveals that the Pcl-I is characterised by elevated Nb (>43 wt.% Nb_2O_5), depletion in Ti and Ca (8.0–8.2 wt.% TiO_2; 6.6–9.3 wt.% CaO) contents compared to Pcl-II (31.8–37.6 wt.% Nb_2O_5; 11.5–15.0 wt.% TiO_2; 9.89–11.0 wt.% CaO) (Table 1, Figs 4, 6a). Consequently, Pcl-II ($Nb^{\#}$: 64–57 mol.%; $Ti^{\#}$: 36–43 mol.%; Table 1) are enriched in the betafite component relative to Pcl-I ($Nb^{\#}$: 78–77 mol.%; $Ti^{\#}$: 22–23 mol.%; Table 1). In general, Pcl-I have low Ba contents compared to the Pcl-II, and in some Pcl-II, BaO can reach 6.5 wt.% (Table 1; compositions 9–11). In general, Pcl-II are relatively enriched in Sr and Pb compared to the associated Pcl-I. However, the distribution of these elements is heterogeneous and if present reaches 0.9 wt.% SrO and 1.7 wt.% PbO, respectively (Table 1). Characteristically, most of the Pcl-I and Pcl-II contain negligible amounts of Ta, Na and F. In some Pcl-II, the Na_2O and F contents reach a maximum of 1.9 and 0.6 wt.%, respectively (Table 1; compositions 12, 13). Pcl-I has a relatively greater proportion of *A*-site vacancies (0.37–0.71 apfu) than the Pcl-II (0.10-0.33 apfu).

Pyrochlore-III

In terms of Nb–Ti contents, Pcl-III is transitional to Pcl-I and Pcl-II, with intermediate pyrochlore and betafite molecular proportions ($Nb^{\#}$: 72–67 mol.%; $Ti^{\#}$: 28–33 mol.%; Table 1). These pyrochlore generally occur in two textural modes, as intermediate-AZ areas within Pcl-II (Fig. 5b,e) and seldom as discrete grains (Fig. 5c,d). Compositionally, Pcl-III are enriched in Nb and U (38.9–40.2 wt.% Nb_2O_5; 26.4–27.8 wt.% UO_2) (Table 1), and depleted in Ti and Ca (9.2–11.8 wt.% TiO_2; 8.7–10.3 wt.% CaO) compared to Pcl-II. Compared to the Pcl-I and -II, these pyrochlore are relatively U-poor, and the UO_2 content is restricted to a narrow compositional range of 26.4–27.8 wt.% (0.43–0.49 apfu; Table 1). However, Pcl-III have relatively higher concentrations of Sr (1.7–2.3 wt.% SrO) and Pb (1.6–2.1 wt.% PbO) compared to most of the Pcl-I and Pcl-II, whereas Na and Ba contents are comparable to those of the Pcl-II.

Pyrochlore-IV

With respect to their composition, these pyrochlore are very similar to the Pcl-II and differ only in their textural mode of occurrence. Pcl-IV commonly occur as discrete grains not associated with other pyrochlore types (Fig. 5c,f,g). The characteristic textural feature that differentiates Pcl-IV from other pyrochlore is the presence of compositional rhythmic zonation (Fig. 5f). This zoning reflects variation in U concentration, with the high-AZ bands enriched in U. Accurate compositions cannot be determined due to the small size of these high-AZ bands. However, analyses with a beam rastered over an area of 100 μm^2, including the high-AZ regions indicate that the U-concentration is very high (>42 wt.% UO_2). These U-enriched bands are very similar in their appearance to primary zoning (Hogarth *et al.*, 2000; Chakhmouradian and Mitchell, 2002; Zurevinski and Mitchell, 2004), but appear to have been intricately folded, perhaps due to post-formational deformational event(s). These pyrochlore commonly contain inclusions of thorite and galena (Fig. 5c,f). Compared to other pyrochlore types, Pcl-IV are relatively enriched in Ti (12.1–15.5 wt.% TiO_2), which is reflected in their higher betafite component ($Nb^{\#}$: 65–55 mol.%; $Ti^{\#}$: 34–45 mol.%; Table 2). Concentrations of all other elements such as Ca, Ba, Pb and Sr are comparable to Pcl-II.

Pyrochlore-V

Back-scattered electron imagery reveals that Pcl-V are altered extensively and characterised by heterogeneously distributed

https://doi.org/10.1180/mgm.2021.6 Published online by Cambridge University Press

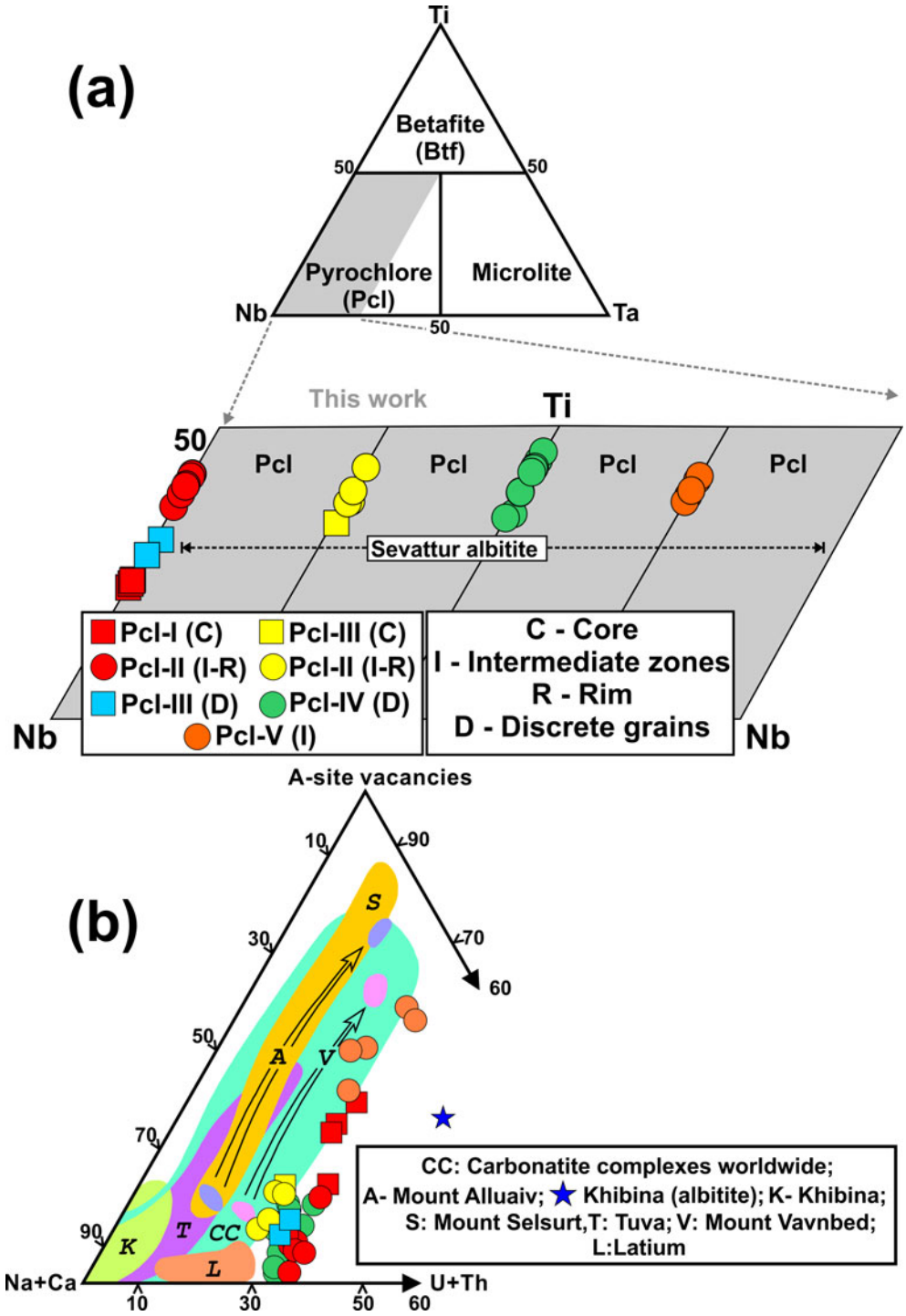

Fig. 3. (a) Compositional variation of the *B*-site cations (apfu) of different pyrochlore generations from the Sevattur albitite. Note the progressive Ti enrichment from core to rim and also in the late generation pyrochlore (Pcl-II to Pcl-V). The solid squares and corresponding solid circles of the same colour represent core (C) and rim (R) compositions respectively. Individual solid square and circle represent either discrete (D) or intermediate (I) zone compositions. (b) Variation in major *A*-site cations and *A*-site vacancies (apfu%) in different U-rich pyrochlore from the Sevattur albitite. U-rich pyrochlore from other albitite and carbonatite occurrences are also plotted for comparison (modified after Chakhmouradian and Mitchell, 2002). Note that the high U content in all the pyrochlore of the Sevattur albitite compared to other occurrences of U-rich pyrochlore from diverse lithologies.

high- and low-AZ areas compared to all other pyrochlore types (Figs 5h,i; 6b). The most significant textural feature of Pcl-V is that the orbicular mantles are disrupted, and numerous fractures are developed (Fig. 5h,i). The high-AZ areas are characterised by elevated Ba content with BaO reaching up to 16.3 wt.% (Table 2). In contrast, the low-AZ areas have a similar composition to that of Pcl-IV with comparable concentrations of U, Nb and Ti (Table 2). Unlike other pyrochlore types, Pcl-V are relatively enriched in Si (2.8–3.9 wt.% SiO_2), Fe (0.4–3.2 wt.% FeO) and exceptionally depleted in Ca (2.7–7.1 wt.% CaO) (Table 2).

https://doi.org/10.1180/mgm.2021.6 Published online by Cambridge University Press

Table 1. Representative pyrochlore (I, II and III) compositions.

Wt. %	1	2	3	4	5	6	7	8	9	10	11	12	13	14	15	16	17	18
Na_2O	0.15	bdl	0.97	0.67	0.71	0.65	0.83	0.66	bdl	bdl	0.86	1.88	1.28	1.73	0.81	1.39	1.18	0.97
K_2O	0.11	0.13	0.11	bdl	bdl	bdl	bdl	0.12	bdl	0.21	bdl	bdl	bdl	bdl	bdl	bdl	bdl	bdl
CaO	8.84	9.25	8.61	6.64	11.48	11.11	11.43	11.10	9.85	11.50	9.51	11.34	10.71	10.67	10.83	9.42	8.73	10.27
MnO	0.37	0.26	0.19	bdl	0.66	0.53	0.46	0.69	0.62	0.66	bdl	bdl	0.11	0.11	0.23	bdl	bdl	0.21
FeO	0.30	0.15	0.42	bdl	0.43	0.36	0.42	0.84	0.61	0.58	bdl	bdl	0.19	0.24	0.14	bdl	bdl	0.21
SrO	bdl	bdl	bdl	bdl	bdl	bdl	bdl	bdl	bdl	bdl	0.86	1.10	1.19	0.82	1.37	2.30	2.12	1.70
BaO	3.08	4.23	3.21	0.93	4.87	5.36	5.34	5.98	7.83	7.32	6.50	2.00	2.30	2.01	3.56	6.20	7.25	3.02
PbO	bdl	bdl	bdl	bdl	bdl	bdl	bdl	bdl	bdl	bdl	2.09	1.80	2.86	1.74	1.72	1.58	2.09	1.88
Y_2O_3	bdl	bdl	bdl	bdl	bdl	bdl	bdl	bdl	bdl	bdl	bdl	bdl	bdl	0.13	bdl	bdl	bdl	bdl
Ce_2O_3	bdl	bdl	bdl	bdl	bdl	bdl	bdl	bdl	bdl	bdl	bdl	0.28	0.26	bdl	0.62	bdl	bdl	0.36
Pr_2O_3	bdl	bdl	bdl	bdl	bdl	bdl	bdl	bdl	bdl	bdl	bdl	0.20	bdl	bdl	0.10	bdl	bdl	bdl
Nd_2O_3	bdl	bdl	bdl	bdl	bdl	bdl	bdl	bdl	bdl	bdl	bdl	0.26	0.36	0.29	0.16	bdl	bdl	0.24
ThO_2	bdl	bdl	bdl	bdl	bdl	bdl	bdl	bdl	bdl	bdl	0.49	1.32	1.52	1.16	2.03	1.20	bdl	1.17
UO_2	32.33	31.70	35.72	34.17	34.10	34.43	33.25	33.85	32.26	32.16	32.99	27.28	26.14	28.09	26.59	27.42	27.80	26.42
Al_2O_3	bdl	bdl	bdl	bdl	0.27	0.46	0.38	0.62	bdl	bdl	bdl	bdl	bdl	bdl	bdl	bdl	bdl	bdl
SiO_2	bdl	bdl	bdl	bdl	0.65	0.76	0.98	bdl	bdl	bdl	bdl	bdl	bdl	bdl	0.41	bdl	bdl	0.15
TiO_2	7.94	8.12	8.04	8.16	13.63	13.33	13.57	11.45	12.85	13.06	12.57	13.22	13.30	13.64	15.03	10.23	9.22	11.83
Nb_2O_5	46.42	45.65	43.56	44.73	32.66	31.77	32.88	34.37	35.21	33.48	32.58	37.63	38.51	36.30	33.97	38.87	40.21	39.64
Ta_2O_5	bdl	bdl	bdl	bdl	bdl	bdl	bdl	bdl	bdl	bdl	bdl	0.88	0.53	0.30	0.23	0.70	bdl	0.42
F	bdl	bdl	bdl	bdl	bdl	bdl	bdl	bdl	bdl	bdl	bdl	0.62	0.51	0.50	0.41	bdl	bdl	0.39
O≡F	-	-	-	-	-	-	-	-	-	-	-	0.26	0.21	0.21	0.17	-	-	0.16
Total	99.54	99.49	100.83	97.79	99.46	98.76	99.54	99.68	99.23	98.97	98.45	99.54	99.56	97.51	98.01	99.31	98.60	98.73
Formula based on ΣB cations = 2																		
Na	0.02	-	0.15	0.10	0.11	0.10	0.12	0.10	-	-	0.14	0.27	0.18	0.25	0.12	0.21	0.18	0.14
K	0.01	0.01	0.01	-	-	-	-	0.01	-	0.02	-	-	-	-	-	-	-	-
Ca	0.70	0.74	0.72	0.54	0.95	0.93	0.92	0.95	0.82	0.98	0.84	0.89	0.83	0.85	0.85	0.79	0.74	0.81
Mn	0.02	0.02	0.01	-	0.04	0.04	0.03	0.05	0.04	0.04	-	-	0.01	0.01	0.01	-	-	0.01
Fe^{2+}	0.02	0.01	0.03	-	0.03	0.02	0.03	0.06	0.04	0.04	-	-	0.01	0.01	0.01	-	-	0.01
Sr	-	-	-	-	-	-	-	-	-	-	0.04	0.05	0.05	0.04	0.06	0.10	0.10	0.07
Ba	0.09	0.12	0.10	0.03	0.15	0.16	0.16	0.19	0.24	0.23	0.21	0.06	0.07	0.06	0.10	0.19	0.23	0.09
Pb	-	-	-	0.05	-	-	-	-	-	-	0.05	0.04	0.06	0.03	0.03	0.03	0.04	0.04
Y	-	-	-	-	-	-	-	-	-	-	-	-	-	0.01	-	-	-	-
Ce	-	-	-	-	-	-	-	-	-	-	-	0.01	0.01	-	0.02	-	-	0.01
Pr	-	-	-	-	-	-	-	-	-	-	-	0.01	-	-	-	-	-	-
Nd	-	-	-	-	-	-	-	-	-	-	-	0.01	0.01	0.01	-	-	-	0.01
Th	-	-	-	-	-	-	-	-	-	-	0.01	0.02	0.03	0.02	0.03	0.02	-	0.02
U	0.53	0.53	0.62	0.58	0.58	0.60	0.56	0.60	0.56	0.57	0.61	0.45	0.42	0.47	0.43	0.48	0.49	0.43
ΣA	1.39	1.43	1.64	1.30	1.86	1.85	1.82	1.96	1.70	1.88	1.90	1.81	1.68	1.76	1.66	1.82	1.78	1.64
□A	0.61	0.57	0.36	0.70	0.14	0.15	0.18	0.04	0.30	0.12	0.10	0.19	0.32	0.24	0.34	0.18	0.22	0.36
Al	-	-	-	-	0.02	0.04	0.03	0.06	-	-	-	-	-	-	-	-	-	-
Si	-	-	-	-	0.05	0.06	0.08	-	-	-	-	-	-	-	0.03	-	-	0.01
Ti	0.44	0.46	0.47	0.47	0.79	0.78	0.77	0.69	0.76	0.79	0.78	0.73	0.73	0.77	0.83	0.60	0.55	0.66
Nb	1.56	1.54	1.53	1.53	1.14	1.12	1.12	1.25	1.24	1.21	1.22	1.25	1.26	1.23	1.13	1.38	1.45	1.32
Ta	-	-	-	-	-	-	-	-	-	-	-	0.02	0.01	-	0.01	0.02	-	0.01
ΣB	2.00	2.00	2.00	2.00	2.00	2.00	2.00	2.00	2.00	2.00	2.00	2.00	2.00	2.00	2.00	2.00	2.00	2.00
F	-	-	-	-	-	-	-	-	-	-	-	0.14	0.12	0.12	0.09	-	-	0.09
O (calc)	6.70	6.72	6.93	6.59	6.94	6.93	6.86	7.00	6.89	7.00	7.00	6.70	6.61	6.68	6.63	6.93	6.91	6.66
Mol.% of end-members																		
$Nb^{\#}$	78	77	77	77	59	59	59	64	62	61	61	62	63	62	57	69	72	67
$Ta^{\#}$	-	-	-	-	-	-	-	-	-	-	-	1	1	-	-	1	-	-
$Ti^{\#}$	22	23	23	23	41	41	41	36	38	39	39	37	36	38	43	30	28	33

1–4: pyrochlore-I; 5–15: pyrochlore-II; 16–18: pyrochlore-III. End-members of pyrochlore supergroup: $Nb^{\#}$-pyrochlore, $Ta^{\#}$-microlite, $Ti^{\#}$-betafite.
bdl: below detection limit; Compositions 1–3, 5–15, 18: WD electron microprobe (IIT Roorkee) and 4, 6 and 7: ED X-ray spectrometry (Lakehead University).

Towards the rim, some very low-AZ areas (Fig. 5h) are found with high Si concentration (>24 wt.% SiO_2), whereas Nb and U concentrations are notably low (Table 2; composition 33) compared to other pyrochlore types.

Pyrochlore nomenclature

The pyrochlore classification has evolved from the 'dominant constituent rule' to the 'dominant valence rule' at a given crystallographic site (Hogarth, 1977; Nickel, 1992; Nickel and Grice, 1998; Hatert and Burke, 2008; Atencio *et al.*, 2010; Christy and Atencio, 2013). According to the present Commission on New Minerals, Nomenclature and Classification (CNMNC) of the International Mineralogical Association (IMA) approved classification of the pyrochlore supergroup, the individual species are defined on the basis of the dominant valence rule at the *Z* site (F, H_2O; OH^-; □) and *A*-site occupancy, respectively (Atencio *et al.*, 2010; Christy and Atencio, 2013). Consequently, many earlier proposed pyrochlore species are considered redundant and are replaced by new species such as fluornatropyrochlore, oxynatropyrochlore, fluorstrontiopyrochlore, etc. (Atencio *et al.*, 2010). Many problems have become evident with the IMA nomenclature

https://doi.org/10.1180/mgm.2021.6 Published online by Cambridge University Press

Table 2. Representative pyrochlore (Pcl-IV and Pcl-V) compositions.

Wt. %	19	20	21	22	23	24	25	26	27	28	29	30	31	32	33
Na_2O	1.55	1.23	1.00	0.78	0.72	1.05	1.27	1.69	1.33	0.68	bdl	0.84	0.53	bdl	bdl
K_2O	bdl	bdl	bdl	bdl	bdl	bdl	bdl	bdl	bdl	0.18	bdl	0.10	0.17	bdl	0.12
CaO	11.48	10.82	11.06	9.61	9.02	10.03	10.50	10.50	10.97	5.58	2.81	5.82	7.13	2.69	5.24
MnO	bdl	0.13	0.30	bdl	bdl	bdl	0.49	bdl	bdl	0.10	0.87	0.43	0.33	0.69	bdl
FeO	0.12	bdl	0.27	0.67	0.31	bdl	0.39	bdl	bdl	2.16	0.44	1.61	3.18	0.77	1.13
SrO	bdl	bdl	bdl	1.48	1.38	1.92	1.97	0.66	1.32	bdl	bdl	bdl	bdl	bdl	bdl
BaO	4.54	5.86	5.05	6.48	7.96	5.59	6.18	4.86	4.82	3.09	15.93	4.47	2.27	16.33	7.50
PbO	bdl	bdl	bdl	2.26	1.02	1.94	1.53	2.12	1.96	bdl	bdl	bdl	bdl	bdl	bdl
ThO_2	bdl	bdl	bdl	1.40	bdl	1.01	1.33	1.93	0.94	bdl	bdl	bdl	bdl	bdl	bdl
UO_2	32.79	32.14	32.49	30.52	32.11	28.96	30.09	31.36	31.46	33.26	28.40	29.05	32.16	30.19	15.12
Al_2O_3	0.38	0.62	0.45	bdl	bdl	bdl	bdl	bdl	bdl	0.83	0.83	0.93	0.71	0.88	2.72
SiO_2	0.12	1.01	0.56	2.05	3.05	bdl	0.91	bdl	bdl	3.58	2.75	3.89	3.39	3.33	24.23
TiO_2	15.46	15.48	14.75	12.12	12.72	11.26	12.67	14.68	12.87	13.38	13.69	12.45	13.76	12.32	11.11
Nb_2O_5	33.49	31.61	33.42	32.75	29.86	35.20	34.11	33.63	34.87	37.22	33.09	36.17	34.22	33.00	23.88
Ta_2O_5	bdl	bdl	bdl	bdl	bdl	0.71	bdl	bdl	bdl	bdl	bdl	bdl	bdl	bdl	bdl
F	bdl	bdl	bdl	bdl	bdl	bdl	bdl	bdl	bdl	bdl	bdl	bdl	bdl	bdl	bdl
O≡F	-	-	-	-	-	-	-	-	-	-	-	-	-	-	-
Total	100.06	98.97	99.44	100.12	98.15	97.67	101.44	101.43	100.54	100.06	98.96	95.76	97.88	100.32	90.69
Formula based on ΣB cations = 2															
Na	0.22	0.17	0.14	0.12	0.11	0.17	0.19	0.25	0.20	0.08	-	0.11	0.07	-	-
K	-	-	-	-	-	-	-	-	-	0.01	-	0.01	0.01	-	-
Ca	0.90	0.84	0.87	0.79	0.74	0.87	0.87	0.86	0.92	0.38	0.21	0.41	0.51	0.20	0.24
Mn	-	0.01	0.02	-	-	-	0.03	-	-	0.01	0.05	0.02	0.02	0.04	-
Fe^{2+}	0.01	-	0.02	0.04	0.02	-	0.03	-	-	0.11	0.03	0.09	0.18	0.05	0.04
Sr	-	-	-	0.07	0.06	0.09	0.09	0.03	0.06	-	-	-	-	-	-
Ba	0.13	0.17	0.15	0.20	0.24	0.18	0.19	0.15	0.15	0.08	0.43	0.11	0.06	0.45	0.13
Pb	-	-	-	0.05	0.02	0.04	0.03	0.04	0.04	-	-	-	-	-	-
Th	-	-	-	0.02	-	0.02	0.02	0.03	0.02	-	-	-	-	-	-
U	0.53	0.52	0.53	0.52	0.55	0.52	0.52	0.53	0.55	0.47	0.44	0.42	0.48	0.47	0.15
ΣA	1.79	1.71	1.73	1.81	1.74	1.89	1.97	1.89	1.94	1.14	1.16	1.17	1.33	1.21	0.56
□A	0.21	0.29	0.27	0.19	0.26	0.11	0.03	0.11	0.06	0.86	0.84	0.83	0.67	0.79	1.44
Al	0.03	0.05	0.04	-	-	-	-	-	-	0.06	0.07	0.07	0.05	0.07	0.14
Si	0.01	0.07	0.04	0.16	0.24	-	0.07	-	-	0.23	0.19	0.25	0.23	0.23	1.04
Ti	0.85	0.84	0.81	0.70	0.73	0.69	0.74	0.84	0.76	0.64	0.71	0.61	0.69	0.65	0.36
Nb	1.11	1.04	1.11	1.14	1.03	1.29	1.19	1.16	1.24	1.07	1.03	1.07	1.03	1.05	0.46
Ta	-	-	-	-	-	0.02	-	-	-	-	-	-	-	-	-
ΣB	2.00	2.00	2.00	2.00	2.00	2.00	2.00	2.00	2.00	2.00	2.00	2.00	2.00	2.00	2.00
F	-	-	-	-	-	-	-	-	-	-	-	-	-	-	-
O (calc)	6.75	6.62	6.71	6.87	6.75	7.00	7.00	6.91	7.00	6.07	6.07	6.03	6.24	6.16	4.88
Mol.% of end-members															
$Nb^{\#}$	57	55	58	62	59	65	62	58	62	63	59	64	60	62	56
$Ta^{\#}$	-	-	-	-	-	1	-	-	-	-	-	-	-	-	-
$Ti^{\#}$	43	45	42	38	41	34	38	42	38	37	41	36	40	38	44

19–27: pyrochlore-IV; 28–33: pyrochlore-V. End-members of pyrochlore supergroup: $Nb^{\#}$-pyrochlore, $Ta^{\#}$-microlite, $Ti^{\#}$-betafite.
bdl: below detection limit; Compositions 19–21, 28–33: WD electron microprobe (IIT Roorkee) and 22–27: ED X-ray spectrometry (Lakehead University).

when used for practical petrological applications without crystallographic data. These are particularly problematic with the incorporation of vacancies (□) in the nomenclature scheme, resulting in species such as uranpyrochlore, bariopyrochlore and strontiopyrochlore all being grouped as 'zero-valence-dominant' pyrochlore (Atencio *et al.*, 2010; Christy and Atencio, 2013). Unfortunately, this approach eliminates the basic petrogenetic compositional information that was evident using the nomenclature scheme of Hogarth (1977) and does not facilitate comparisons with previous paragenetic studies of pyrochlore in carbonatites and alkaline rocks. Hence, the Hogarth (1977) nomenclature is superior to the IMA scheme for most petrogenetic purposes. The major shortfall of the existing IMA classification is that, except for F, the anions (i.e. O^{2-}, OH^-) and H_2O cannot be determined using common analytical methods such as electron microprobe analysis. Although, Raman microspectroscopy can provide information on the presence or absence of OH^-, H_2O, etc., their distribution in the different sites (*A* or *Z*) can only be quantified by the single-crystal X-ray diffraction (XRD) studies. These are not practical for most naturally occurring pyrochlore.

Regardless of having a very high U concentration and a substantial compositional difference between Pcl-I to Pcl-IV, it is disappointing to note that the IMA classification would compel us to regard all of them as 'oxycalciopyrochlore' (ideally, $Ca_2Nb_2O_7$). The classification of Pcl-V is even more problematic owing to the presence of *A*- and *Z*-site vacancies (Table 2). For these pyrochlore, three different species could be possible: hydro/kenopyrochlore (Table 2; compositions 29, 30), kenopyrochlore (Table 2; compositions 28, 32) and hydro/kenocalciopyrochlore (Table 2; compositions 31). However, following the 'Site Total Charge (STC)' method of Bosi *et al.* (2019) the charge balanced end-member of the hydro/kenocalciopyrochlore must contain OH^- at the *Z* site [anionic group: $(O_6^{2-}OH^-)^{13-}$]; and thus can be

https://doi.org/10.1180/mgm.2021.6 Published online by Cambridge University Press

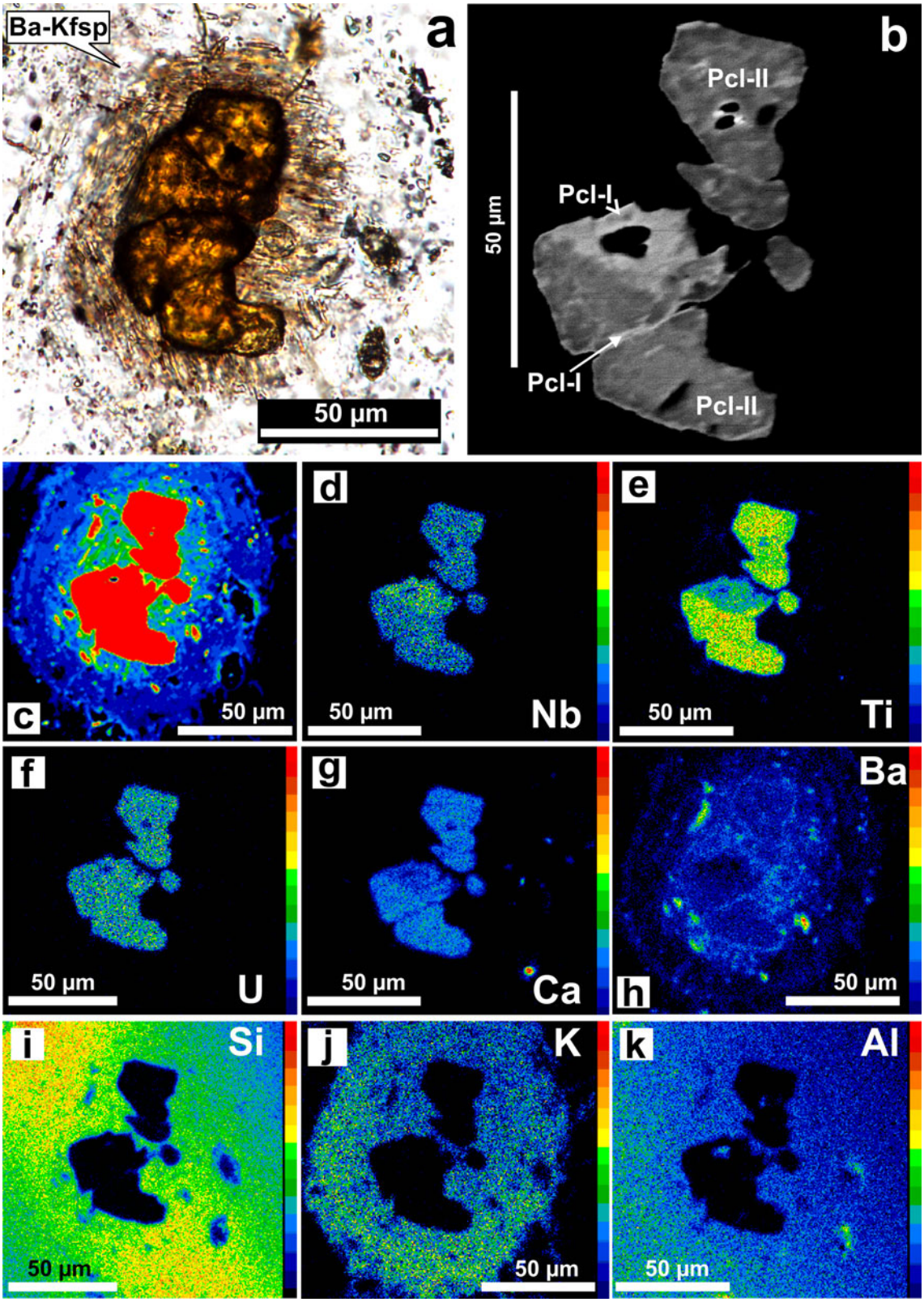

Fig. 4. (a) Transmitted (PP – plane polarised) light photomicrograph showing extremely U-rich pyrochlore set within an albite matrix. Note the discolouration at the grain margin. (b) BSE image of the same pyrochlore grain in (a) illustrates a high-AZ relict core of Pcl-I altered to Pcl-II (low-AZ areas). Note the discrete Pcl-II shows patchy zoning and lacks the high-AZ core. (c) False-colour BSE image showing textural details of Pcl-I and Pcl-II. The Ba-rich potassium feldspar mantle is represented by the blue colour circular area enveloping the pyrochlore. (d–k) X-ray maps illustrating the distribution of elements: (d) Nb, (e) Ti, (f) U, (g) Ca, (h) Ba, (i) Si, (j) K and (k) Al between Pcl-I and Pcl-II. A considerable variation in Nb, Ti and Ca between Pcl-I and Pcl-II is visible. Enrichment of Si, Al, K and Ba in the orbicular mantle is also noticeable. Bright green spots in the Ba map (h) represent tiny baryte crystals within the orbicular mantle.

https://doi.org/10.1180/mgm.2021.6 Published online by Cambridge University Press

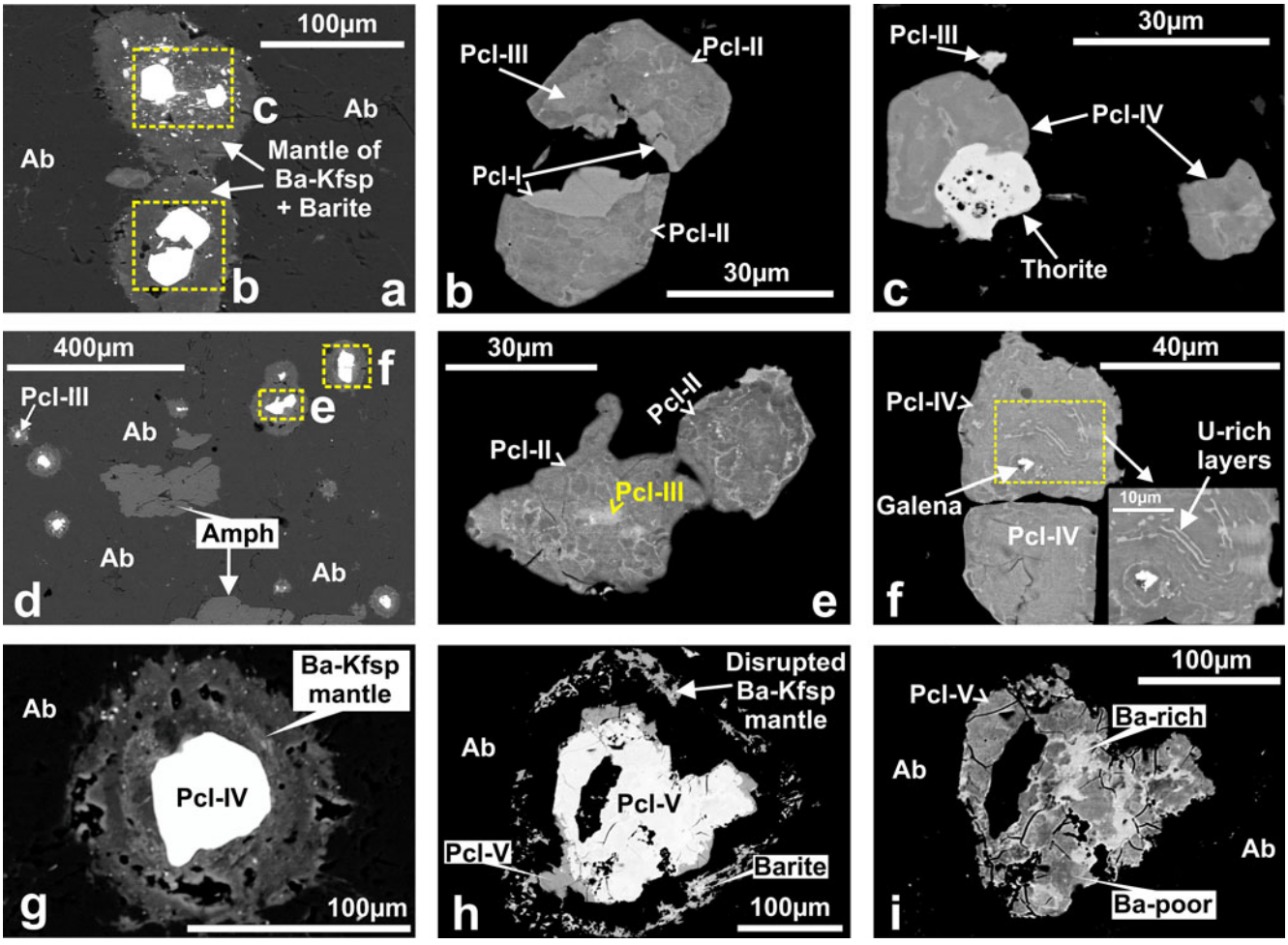

Fig. 5. Back-scattered electron images (BSE) illustrating textural and compositional variations of pyrochlore-group minerals occurring in Sevattur albitites. (a) BSE image showing the overall textures pertaining to the pyrochlore (high-AZ crystals). Note the Ba-rich potassium feldspar (Low-AZ) mantling the pyrochlore. (b) Enlarged view of U-rich pyrochlore with a high-AZ relict core (Pcl-I) in association with Pcl-II and Pcl-III. Note that the variable AZ in Pcl-II and Pcl-III illustrates patchy zoning. (c) Altered pyrochlore (Pcl-IV) in association with thorite. A small discrete crystal of Pcl-III is also present. (d) Amphibole and pyrochlore are set within an albite matrix. (e) A different textural variant of Pcl-II with extensive patchy zoning. Note variable high-AZ regions (Pcl-III) of different composition to that of Pcl-I and Pcl-II. Such Pcl-III are designated as transitional pyrochlore with intermediate betafite molecular proportions (see text) (f) U-rich bands in Pcl-IV similar to a relic primary oscillatory zoning with an inclusion of galena. (g) A different textural mode of occurrence of Pcl-IV with no visible zoning. Note that the orbicular mantle also shows variable AZ originating from variation in Ba content in the potassium feldspar. (h) Highly metamictised Pcl-V with a disrupted mantle. Low-AZ area at the bottom left corner is characterised by a low analytical total: a sign of U mobility. (i) High contrast BSE image of the same Pcl-V as illustrated in (h) showing extremely Ba-rich high-AZ areas. Note numerous fractures running from rim to core and connected to the Ba-rich zones.

re-classified as hydroxykeno/hydrocalciopyrochlore. To avoid such complicated proliferations in the nomenclature, as well for the better representation of the compositional variability, we have used a much simpler nomenclature scheme where Pcl-I to Pcl-IV are referred to as U-rich pyrochlore and some of the Pcl-V as U–Ba-rich pyrochlore. To emphasise the Nb–Ti variations in our data, we limit our representation of pyrochlore compositions to within the Nb–Ta–Ti solid-solution field. Thus, representing all our data in terms of pyrochlore–betafite–microlite solid-solutions molecular proportions (Tables 1, 2), seems logical as *B*-site Nb–Ta–Ti are the primary classificatory parameters for distinguishing these end-members. The absence of information on the specific anionic groups, H_2O, and vacancies restricts the use of prefixes such as 'oxy', 'hydro', 'keno', etc. (Atencio *et al.*, 2010). It is worthwhile to note that according to the previous nomenclature of the pyrochlore group (Hogarth, 1977), except for Pcl-I and Pcl-III (uranpyrochlore) all of the pyrochlore (Pcl-II, -IV, and -V) are betafite. This is reflected in the increasing betafite molecular proportion for Pcl-II to Pcl-V relative to Pcl-I (Tables 1, 2).

Orbicular mantle, matrix and other mineral compositions

The orbicular mantles around the pyrochlore (Figs 2d; 5a) are essentially potassium feldspar ($KAlSi_3O_8$) with variable celsian ($BaAl_2Si_2O_8$) proportions having BaO contents ranging up to 8.0 wt.% (Table 3). The composition ranges from $Or_{85}Ab_2Cs_{13}$ to $Or_{98}Cs_2$ (where Or = orthoclase, Ab = albite and Cs = celsian) (Table 3; compositions 3, 4). Isolated discrete potassium feldspars are seldom present within the albite matrix (Fig. 2g). BSE imagery reveals that such discrete, isolated crystals are characterised by high- and low-AZ zones. The high-AZ zones are enriched in Ba (>6.5 wt.% BaO), and the low-AZ areas are represented by albite–K-feldspar solid solution ($Ab_{66}Or_{31}Cs_3$) with a low Ba content (1.6 wt.% BaO; Table 3; composition 7). The boundaries between the high- and low-AZ zones are gradational and irregular

https://doi.org/10.1180/mgm.2021.6 Published online by Cambridge University Press

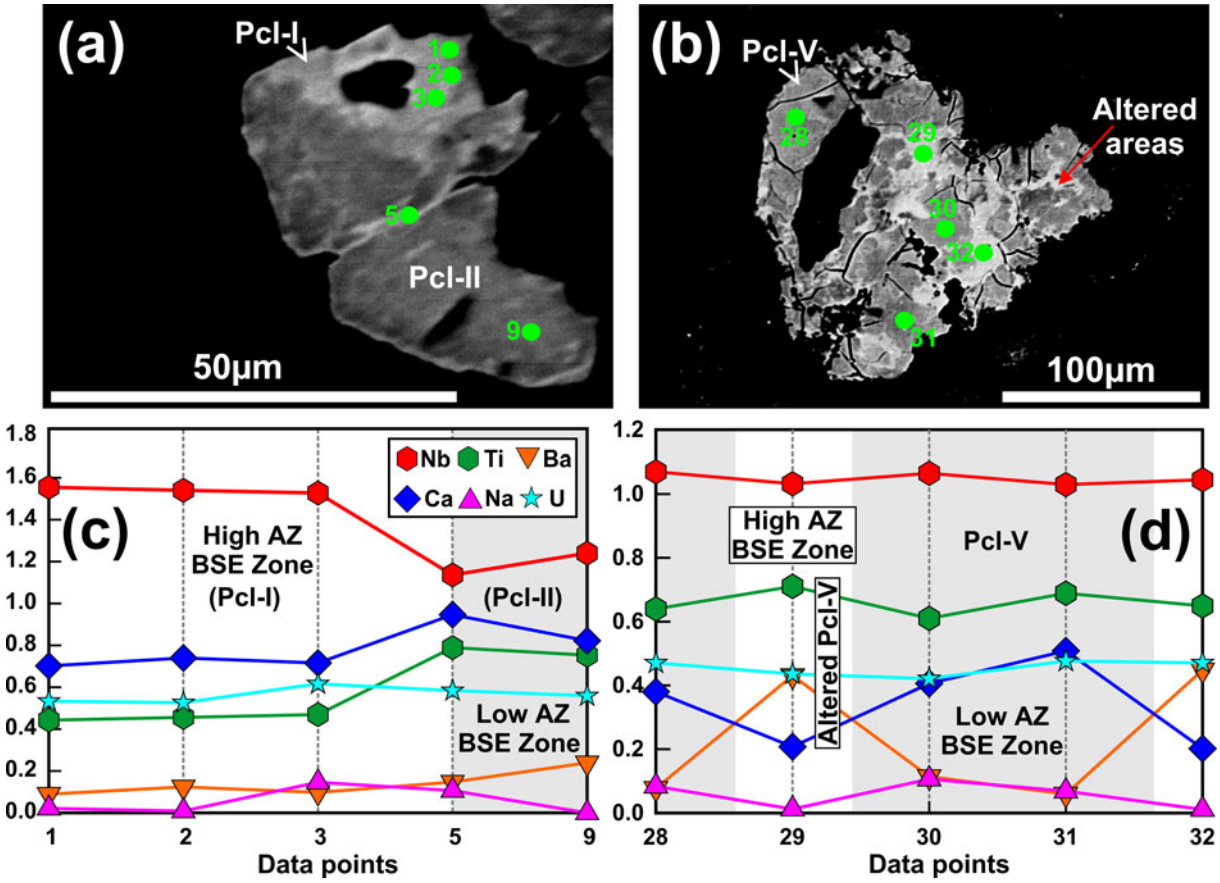

Fig. 6. (a–b) Back-scattered electron images of Pcl-I, Pcl-II and Pcl-V. Analytical points are marked. (c) Compositional variation between Pcl-I and Pcl-II in (a) demonstrates an increase in Ti, Ca and a significant decrease in Nb concentration at constant U content. (d) Compositional variation between high- and low-AZ regions within metamict Pcl-V in (b), illustrating high Ba enrichment in high-AZ regions. Note a strong negative correlation between Ba and Ca in high-AZ regions.

(Fig. 2g). The feldspar composition ranges from the relict K-feldspar ($Or_{98}Cs_2$) to the pure albite (Ab_{100}) of the matrix through an intermediate composition of $Or_{31}Ab_{66}Cs_3$ (Table 3). Such features indicate that the potassic feldspars predate the albite matrix and there is a partial replacement of K by Na and Ba. Compositionally, the Ba-rich potassic feldspars could be hyalophane [$(K,Ba)Al(Si,Al)_3O_8$]; an intermediate member of orthoclase–celsian solid-solution series. In general, the Ba–K–Na feldspars can occur in geochemical milieus ranging from authigenic or hydrothermal to igneous and metamorphic (Essene *et al.*, 2005; Raith *et al.*, 2014). Among the igneous rocks, they are quite common in feldspathoidal alkaline rocks such as leucitites and basanites (Zhang *et al.*, 1993; Naushad *et al.*, 2019). However, with respect to hyalophane (*sensu stricto*), the celsian molecular proportion is usually high (>23.5 mol.%) and there is extensive solid solution along the celsian–orthoclase join with only limited solid solution towards albite (Essene *et al.*, 2005). Unlike our data, hyalophane (*sensu stricto*) is usually characterised by a low Si and relatively higher Al contents compared to the Ba-rich K-feldspars. Thus, these mantled feldspars are better termed as 'Ba-bearing K-feldspar', rather than hyalophane. Pure baryte (65.8 wt.% BaO; 33.7 wt.% SO_3) is found commonly within the orbicular mantles (Fig. 4h). In places, baryte is found associated with discrete Ba-bearing K-feldspar (Fig. 2g). The matrix composition is rather uniform and composed essentially of pure albite (Table 3).

Calcite, with very low Mg and Fe contents (Table 4) in the albitite is a relatively late-stage mineral confined to interstices between previously formed minerals. The silicate-rich blue carbonatite is essentially a dolomite carbonatite, and pure calcite is rarely present as a relict phase. The dolomite composition in the blue carbonatite is variable, evolving from the manganoan dolomite (Table 4; composition 5) towards ferroan dolomite composition (Table 4; compositions 6–8). Unlike the blue carbonatite, the albitite is devoid of dolomite.

The amphiboles of the albitite are magnesio-riebeckite and ferri-winchite (Table 5). Similar amphiboles are also present in the blue carbonatite together with magnesio-arfvedsonite and aegirine. The mica-group minerals are essentially phlogopite in composition (Table 6). Rare pyrite grains are present within the albite matrix and replaced partially by magnetite. Both pyrite and magnetite are surrounded by potassium feldspar mantles (Fig. 2f).

Discussion

In the Sevattur carbonatites and associated fenites, pyrochlore shows a greater compositional variation compared to those in other carbonatite complexes such as: Meech Lake (Hogarth *et al.*, 2000), Oka (Zurevinski and Mitchell, 2004), Aley (Chakhmouradian *et al.*, 2015), St. Honoré (Mitchell, 2015) and Good Hope (Mitchell *et al.*, 2020) in Canada; Kaiserstuhl,

https://doi.org/10.1180/mgm.2021.6 Published online by Cambridge University Press

Table 3. Representative compositions of feldspar.

	1	2	3	4	5	6	7	8	9	10
Na_2O	0.24	0.11	bdl	0.21	0.16	bdl	7.34	12.01	11.37	11.32
K_2O	14.27	13.89	16.46	13.86	15.53	15.88	5.28	bdl	0.30	bdl
CaO	bdl	bdl	bdl	bdl	bdl	bdl	0.10	bdl	0.44	0.18
FeO	bdl	bdl	bdl	0.53	bdl	bdl	bdl	bdl	bdl	0.10
BaO	6.68	8.03	1.13	7.00	2.18	2.70	1.57	bdl	bdl	bdl
Al_2O_3	20.03	21.12	18.03	19.53	18.16	19.17	21.37	19.04	19.38	19.71
SiO_2	58.55	56.10	64.60	60.59	63.96	62.25	64.08	67.81	67.57	69.86
Total	99.77	99.25	100.22	101.72	99.99	100.00	99.74	98.86	99.06	101.17
Formula based on 8 oxygen atoms										
Na	0.02	0.01	-	0.02	0.01	-	0.64	1.03	0.97	0.94
K	0.89	0.88	0.98	0.84	0.93	0.96	0.30	-	0.02	-
Ca	-	-	-	-	-	-	-	-	0.02	0.01
Fe	-	-	-	0.02	-	-	-	-	-	-
Ba	0.13	0.16	0.02	0.13	0.04	0.05	0.03	-	-	-
Al	1.15	1.23	0.99	1.10	1.00	1.07	1.14	0.99	1.01	1.00
Si	2.85	2.78	3.00	2.89	2.99	2.94	2.89	3.00	2.99	3.01
ΣCations	5.04	5.06	4.99	5.00	4.97	5.02	5.00	5.02	5.01	4.96
Mol.% of end-members										
Or	86	84	98	85	94	95	31	-	2	-
Ab	2	1	-	2	1	-	66	100	96	99
An	-	-	-	-	-	-	-	-	2	1
Cs	12	15	2	13	4	5	3	-	-	-

1, 2, 7: discrete alkali feldspar; 3–6: orbicular mantle; 8–10: matrix feldspar.
bdl: below detection limit.

Germany (Walter *et al.*, 2018); Sokli, Finland (Lee *et al.*, 2006); and Khibina (Zaitsev *et al.*, 2012) and Chuktukon (Chebotarev *et al.*, 2017) in Russia. Regardless of the lithology, U-rich pyrochlore can occur in any of these diverse parageneses with, or without, concomitant Ta-enrichment as seen in many alkaline complexes such as Kaiserstuhl (Badberg nosean syenites), and the Fen complex (magnesiocarbonatites) where primary oscillatory zoned pyrochlore are U–Ta-rich (Hogarth *et al.*, 2000; Walter *et al.*, 2018). In contrast, the NIOCAN and Bond Zone occurrences at the Oka and the Meech Lake calcite carbonatites contain both U–Ta-rich and U-rich–Ta-poor pyrochlore (Hogarth *et al.*, 2000; Zurevinski and Mitchell, 2004). Additionally, pyrochlore rich in U and light REE (LREE) can also form during hydrothermal alteration as found in calcite carbonatite and ankerite carbonatite of the Orberg (Kaisersthul, Germany) and the Belaya Zima alkaline pluton (Russia) (Khromova *et al.*, 2017; Walter *et al.*, 2018).

Compared to carbonatites and other alkaline rocks, only a few occurrences of albitite-hosted pyrochlore have been reported. The well-known examples include Lovozero, Khibina and Tai-Keu, Russia (Chakhmouradian and Mitchell, 2002 and references therein). Except for Khibina, none of the albitite-hosted pyrochlore are as U-rich as those in the Sevattur albitites; rather a broad compositional spectrum was reported ranging from Na–Ca–F-rich pyrochlore, strontiopyrochlore and plumbopyrochlore to ceriopyrochlore (Chakhmouradian and Mitchell, 2002). Thus, it is evident that U-rich pyrochlore can be of either primary or secondary origin.

Pyrochlore compositional and textural features: A comparison between the Sevattur albitites and similar occurrences

In general, U-rich pyrochlore are commonly prone to metamictisation, leading to substantial crystal structure damage. This makes them susceptible to intense alteration which facilitates U mobility (Lumpkin and Ewing, 1995, 1996; Hogarth *et al.*, 2000). At Sevattur, regardless of the very high U content, only a few altered Pcl-V grains exhibit evidence of U mobility, as shown by the introduction of Ba and Si into pyrochlore structure (Table 2; compositions 32, 33). Such features indicate intense alteration compared to other pyrochlore types. Early-formed pyrochlore are characterised typically by oscillatory zoning, with progressive alteration leading to patchy zoning. Such altered pyrochlore are usually marked by diverse areas of low- and high-AZ zones in BSE imagery. Analogous patchy zoning (Fig. 5) is observed in Pcl-II to Pcl-V. Unlike other occurrences, a reverse trend is observed with respect to the hydration and *A*-site cation deficiency from Pcl-I to Pcl-IV, i.e. the early formed Pcl-I having relatively higher proportion of *A*-site vacancies compared to the altered and late-formed Pcl-II to Pcl-IV (Tables 1, 2). The patchy-zoned pyrochlore (Pcl-II to -V) are characterised by an overall Ca and Ti enrichment and Nb depletion compared to the relict Pcl-I at a constant U concentration. Regardless, of the Ca–Ti enrichment, it must be noted that the pattern of patchy zoning observed in Pcl-II to Pcl-IV is quite different from that seen in the Ba-rich Pcl-V. The Pcl-II and -III pyrochlores show micrometre-sized patchy zoning with a limited number of fractures extending – protruding from the rim towards core (Fig. 5b,e).

In contrast, Pcl-V are characterised by broad high-AZ areas which are connected by numerous fractures extending from the cores towards the rim (Fig. 5i). Such textural and compositional features of Pcl-V, together with extensive leaching of Ca, Sr, Pb, and heterogeneous Ba enrichment, suggest that these pyrochlore suffered severe metamictisation and subsequent pervasive alteration. Note that Pcl-I, which is present in association with Pcl-II and Pcl-III, is devoid of any detectable zoning (Fig. 5a). This observation suggests that Pcl-I has formed earlier in the paragenetic sequence of pyrochlore formation (Pcl-II to Pcl-IV).

Development of patchy zoning, together with the low Na, F concentrations and considerable variations in Nb, Ti and Ca contents between Pcl-I and Pcl-II, probably indicate a combination of low-temperature alteration and metamictisation effects (Lumpkin and Ewing, 1995; Hogarth *et al.*, 2000; Zurevinski and Mitchell, 2004). This hypothesis is in accord with the discolouration at grain margins, numerous fractures, and complexly curved

https://doi.org/10.1180/mgm.2021.6 Published online by Cambridge University Press

Table 4. Representative compositions of carbonates.

Wt. %	1	2	3	4	5	6	7	8	9	10
MgO	0.22	0.53	0.58	0.87	16.23	17.75	17.78	17.46	0.99	0.76
CaO	51.76	51.10	51.93	53.24	29.57	29.45	29.84	30.14	50.58	54.14
MnO	0.22	0.68	0.68	0.63	6.50	0.33	0.33	0.31	1.71	0.26
FeO	0.38	0.43	0.31	0.66	0.56	5.07	4.73	6.92	bdl	0.86
SrO	bdl	bdl	bdl	bdl	bdl	0.60	0.41	0.47	0.55	0.94
BaO	bdl	bdl	bdl	bdl	0.13	bdl	bdl	0.02	bdl	0.09
Total	52.58	52.74	53.50	55.40	52.99	53.20	53.09	55.32	53.83	57.05
Molar percentage of carbonate end-members										
$MgCO_3$	0.59	1.40	1.52	2.18	39.09	42.08	42.11	40.26	2.57	1.87
$CaCO_3$	98.53	96.94	97.02	95.99	51.18	50.18	50.79	49.95	94.35	95.63
$MnCO_3$	0.33	1.02	1.00	0.90	8.89	0.44	0.44	0.41	2.52	0.36
$FeCO_3$	0.56	0.64	0.46	0.93	0.76	6.74	6.28	8.95	-	1.19
$SrCO_3$	-	-	-	-	-	0.55	0.38	0.42	0.56	0.90
$BaCO_3$	-	-	-	-	0.08	-	-	0.01	-	0.06

1–4: albitite; 5–10: blue (silicate-rich) carbonatite.
bdl: below detection limit.

concentric zones observed particularly in Pcl-II (Figs 4a,b; 5b,e). Thus, we propose that the patchy zoning in the late generation pyrochlore is due mainly to the combination of metamictisation and hydrothermal alteration processes. This is in accord with the observation of Hogarth *et al.* (2000) that there is little difference in the zonation patterns produced by low-temperature hydrothermal alteration and metamictisation processes, and it is not straightforward to differentiate between these processes. Unlike other U-rich pyrochlore occurrences, metamictisation causes no evident U-mobility, as most of these pyrochlore were protected by the K-feldspar orbicular mantle (see below).

Pyrochlore alteration and related substitutional mechanisms

Pyrochlore-group minerals are susceptible to post-crystallisation alteration and their composition changes during evolution from magmatic to hydrothermal, weathering and supergene, and metamictisation processes (Lumpkin and Ewing, 1995, 1996; Nasraoui and Bilal, 2000; Hogarth *et al.*, 2000; Zurevinski and Mitchell, 2004; Sharygin *et al.*, 2009; Chakhmouradian *et al.*, 2015; Mitchell, 2015). A generalised alteration pattern or trend cannot be deduced, as late-stage alteration processes are very dependent on the local fluid compositions, pH, the host rock composition and its rheological properties. Hence, Mitchell (2015) opined that "all Nb deposits are unique in terms of the pyrochlore compositional variations and their degree of alteration by deuteric fluids" and each should be judged on its own merits. In general, it is observed that alteration usually produces a more hydrated pyrochlore with significant leaching of *A*-site cations such as Na, Ca and U, together with the introduction of large cations (Ba, Sr and K), and in some extreme cases significant LREE-enrichment (Lumpkin and Ewing, 1995; 1996; Hogarth *et al.*, 2000; Zurevinski and Mitchell, 2004; Lee *et al.*, 2006; Chebotarev *et al.*, 2017; Walter *et al.*, 2018). This general trend is not observed for the Sevattur albitite pyrochlore-group minerals. In contrast, significant Ti enrichment is observed in the late-formed pyrochlore (Pcl-II to Pcl-V). Such Ti enrichment, coupled with decreasing Nb content in pyrochlore has been reported for Lovozero albitites, the Katugin alkali granites (Russia) and the Latium (Italy) volcanic province (Chakhmouradian and Mitchell, 2002; Caprilli *et al.*, 2006; Mitchell, 2015; Starikova *et al.*, 2019).

On the basis of compositional variation related to pyrochlore alteration, three different evolutionary trends (primary, transitional and secondary) were proposed by Lumpkin and Ewing (1995; 1996). The primary alteration of pyrochlore is related invariably to the leaching of Na, Ca and F, coupled with increasing *A*- and *O*-site vacancies and in some cases Mn, Sr, Fe enrichment through various coupled substitutions (Lumpkin and Ewing, 1995). The larger proportion of *A*-site vacancies, together with low Na and F contents in Pcl-I, indicate primary alteration where Na and F were leached from the *A* and *Z* sites leading to vacancies at these sites. In contrast, Pcl-II to Pcl-IV are near-stoichiometric pyrochlore with Ca filling the *A* sites.

The substitution mechanisms discussed above do not explain the Ti enrichment and Nb depletion in Pcl-II to Pcl-IV compared to Pcl-I. We observed an excellent Nb+Na *versus* Ti+U correlation between Pcl-I to Pcl-IV through a $3Nb^{5+} + Na^{+} \rightarrow 3Ti^{4+} + U^{4+}$ substitution ($R^2 = 0.95$; Fig. 7a). A similar substitution mechanism was proposed for the extremely U-rich pyrochlore and betafite from the Latium volcanic province (Caprilli *et al.*, 2006), and these pyrochlore-group minerals are also characterised by patchy zoning similar to that of the Sevattur albitite-hosted pyrochlore. This is also in agreement with other U–Ti-rich pyrochlore occurrences (Fig. 7b) demonstrating decreasing Na and Nb with increasing Ti in the late pyrochlore generations (Pcl-II to Pcl-V). Similarly, the Ca–Ti enrichment in Pcl-II to Pcl-IV can be explained by the $2Nb^{5+} \rightarrow 2Ti^{4+} + Ca^{2+}$ substitution ($R^2 = 0.98$; Fig. 7c). With the exception of the Latium volcanic province, this substitution is not well defined for the other U-rich pyrochlore occurrences (Fig. 7d). We consider that all these relationships are primary as there no evidence of hydration and low *A*-, *O*- and *Z*-site vacancies are found in Pcl-II to -IV.

Barium-rich pyrochlore usually forms during hydrothermal or supergene alteration of primary Na–Ca-pyrochlore as seen at Tchivira (Angola); Panda Hill (Tanzania) and Mrima Hill (Kenya) (Jager *et al.*, 1959; Harris, 1965; Traversa *et al.*, 2001; Melgarejo *et al.*, 2012; Chebotarev *et al.*, 2017). In contrast, primary Ba-pyrochlore reported from Araxá with >11 wt.% BaO was replaced subsequently by late-stage Ba-rich pyrochlore along fractures (Mitchell, 2015). Thus, it is crucial to understand whether the Ba-enrichment in pyrochlore is primary or the result of secondary alteration processes.

The Ba-enrichment in Pcl-II to Pcl-V occurred through the $2Nb^{5+} \rightarrow 2Ti^{4+} + Ba^{2+}$ substitution ($R^2 = 0.94$; Fig. 7e). This substitution successfully explains Ba enrichment in all the pyrochlore types, in agreement with other U-rich pyrochlore examples

https://doi.org/10.1180/mgm.2021.6 Published online by Cambridge University Press

Table 5. Representative amphibole compositions.

	1	2	3	4	5
Na_2O	6.66	6.52	7.77	4.68	4.14
K_2O	bdl	bdl	bdl	bdl	0.32
CaO	0.89	0.82	0.81	6.31	6.61
FeO	1.37	bdl	1.78	7.18	6.17
MgO	12.66	13.85	13.85	14.30	14.95
Al_2O_3	0.56	0.82	0.59	1.18	1.13
Fe_2O_3	20.92	20.85	18.68	10.71	10.67
SiO_2	53.75	54.21	54.59	53.16	53.36
TiO_2	bdl	bdl	bdl	bdl	0.11
H_2O*	2.08	2.10	2.11	2.07	2.08
Total	98.88	99.17	100.18	99.60	99.54
Formula based on 23 oxygens					
Na	0.00	0.00	0.26	0.29	0.18
K	0.00	0.00	0.00	0.00	0.06
ΣA	0.00	0.00	0.26	0.29	0.24
Na	1.86	1.80	1.88	1.02	0.98
Mg	0.00	0.05	0.00	0.00	0.00
Ca	0.14	0.13	0.12	0.98	1.02
ΣB	2.00	1.98	2.00	2.00	2.00
Mg	2.72	2.89	2.93	3.08	3.21
Fe^{2+}	0.17	0.00	0.21	0.87	0.74
Fe^{3+}	2.11	2.11	1.86	1.05	1.05
ΣC	5.00	5.00	5.00	5.00	5.00
Al	0.10	0.14	0.10	0.20	0.19
Fe^{3+}	0.15	0.13	0.14	0.12	0.11
Si	7.75	7.73	7.76	7.68	7.69
Ti	0.00	0.00	0.00	0.00	0.01
ΣT	8.00	8.00	8.00	8.00	8.00
ΣCations	15.00	14.98	15.26	15.29	15.24
OH*	2.00	2.00	2.00	2.00	2.00

1–3: magnesio-riebeckite; 4–5: ferri-winchite (species names are after Hawthorne *et al.*, 2012).
Fe^{2+}/Fe^{3+} ratio estimated from stoichiometry (after Droop, 1987).
*H_2O calculated from (F+Cl+OH=2).
bdl: below detection limit.

Table 6. Representative compositions of phlogopite.

	1	2	3	4	5
Na_2O	0.12	bdl	bdl	bdl	bdl
K_2O	9.06	9.37	9.25	9.18	9.32
MgO	18.97	17.74	17.91	18.18	18.23
MnO	bdl	0.13	bdl	bdl	0.11
FeO	12.70	12.42	12.53	12.62	12.49
TiO_2	1.33	1.96	1.72	1.39	1.47
Al_2O_3	11.27	11.95	11.63	11.81	11.31
SiO_2	42.76	43.08	42.84	42.81	43.01
F	0.20	bdl	0.14	bdl	0.18
H_2O*	4.02	4.09	4.00	4.09	3.99
O=F	0.08	-	0.06	-	0.08
Total	100.34	100.74	99.96	100.08	100.03
Formula based on 7 [*Z*(tetrahedral) and *Y*(octahedral)] cations					
Na	0.02	-	-	-	-
K	0.84	0.88	0.87	0.86	0.87
Σ*X*	0.86	0.88	0.87	0.86	0.87
Mg	2.06	1.94	1.97	1.99	2.00
Mn	-	0.01	-	-	0.01
Fe^{2+}	0.78	0.76	0.77	0.77	0.77
Al	0.09	0.18	0.16	0.16	0.14
Ti	0.07	0.11	0.10	0.08	0.08
Σ*Y*	3.00	3.00	3.00	3.00	3.00
Al	0.88	0.84	0.84	0.86	0.84
Si	3.12	3.16	3.16	3.14	3.16
ΣZ	4.00	4.00	4.00	4.00	4.00
ΣCations	7.86	7.88	7.87	7.86	7.87
OH*	1.95	2.00	1.97	2.00	1.96
F	0.05	-	0.03	-	0.04

Phlogopite $[XY_3Z_4O_{10}(OH,F)_2]$ (after Giebel *et al.*, 2019).
*H_2O calculated from (F+Cl+OH=2).
bdl: below detection limit.

(Fig. 7f). Note that the lowest Ba content is found in Pcl-I (Table 1; compositions 4) and some of the late-generation pyrochlore (Pcl-II, -III and -V) also have relatively low Ba contents compared to some of Pcl-I. The very low modal abundance of baryte and Ba-rich potassium feldspars within the orbicular mantle suggests that Ba was introduced to the system by an externally derived Ba-rich fluid. This is in accordance with the observation that the majority of the U–Ta-rich pyrochlore from the associated dolomite and calcite carbonatites are also Ba-rich and associated invariably with baryte. This Ba-enrichment is probably one of the reasons why patchy zoning occurs in most of the late-generation pyrochlore (Pcl-II to Pcl-IV). These substitutions also show a continuous increase in Ca–Ti–Ba contents from the core towards the rim for Pcl-I to Pcl-II and eventually evolved to Pcl-IV and Pcl-V (Fig. 7).

The prominent substitution observed for Pcl-II to Pcl-IV are minor *A*-site and *Z*-site vacancies and occupancy of these sites by Ca and O (calculated empirically from the total cations) (R^2 = 0.93; Fig. 8a). Due to lack of the H_2O, OH and F data, we considered that, other than oxygen, the remainder of the *O* and *Z* sites are vacant, especially for the altered Pcl-V. This substitution also explains the Ca enrichment and near-stoichiometric compositions of Pcl-II to Pcl-IV formation. This is in agreement with other occurrences of the U-rich pyrochlore and betafite from diverse parageneses (Fig. 8b). This substitution also suggests that the highly-altered Ba-rich Pcl-V have suffered additional extensive secondary alteration leading to decreases in the Ca content followed by a substantial increase in vacancies at *A*, *O* and *Z* sites, respectively. Hydration also occurred as evidenced by some of the Pcl-V having relatively low analytical totals compared to other pyrochlore. It is noteworthy that the mantle around Pcl-V is disrupted, thus the Ba-rich fluid had sufficient time to interact with these pyrochlore, causing variable Ba-enrichment at the expense of Ca and Sr. The effect of secondary alteration is also evident with respect to their high Si content relative to the other pyrochlore (Williams *et al.*, 1997; Uher *et al.*, 1998; Dumańska-Słowik *et al.*, 2014). The highly fractured nature of all Pcl-V, with textural features such as the fractures extending from rim towards the core, broad high- and low-AZ BSE zones, points towards a significant role of metamictisation in their alteration.

Plausible genesis of the pyrochlore group minerals

Pyrochlore compositions are useful in delineating their origin using the Ca–Na–*A*-site vacancy ternary plot with respective fields for postulated magmatic, hydrothermal, or weathering and supergene pyrochlore (Nasraoui and Bilal, 2000; Zurevinski and Mitchell, 2004; Fig. 9). Primary magmatic pyrochlore are usually Na–Ca-rich and with progressive alteration, the composition shifts towards postulated hydrothermal (Zurevinski and Mitchell, 2004) and supergene (Nasraoui and Bilal, 2000) fields with significant *A*-site vacancies. Uranium-rich pyrochlore in the Sevattur albite show an unusual trend in which the early-formed Pcl-I plots within the hydrothermal field followed by more betafite-rich Pcl-II to Pcl-IV plotting toward the magmatic field (Fig. 9a). Such a trend is also seen at the Oka carbonatite and Latium volcanic complexes (Fig. 9b). Note that both pyrochlore

https://doi.org/10.1180/mgm.2021.6 Published online by Cambridge University Press

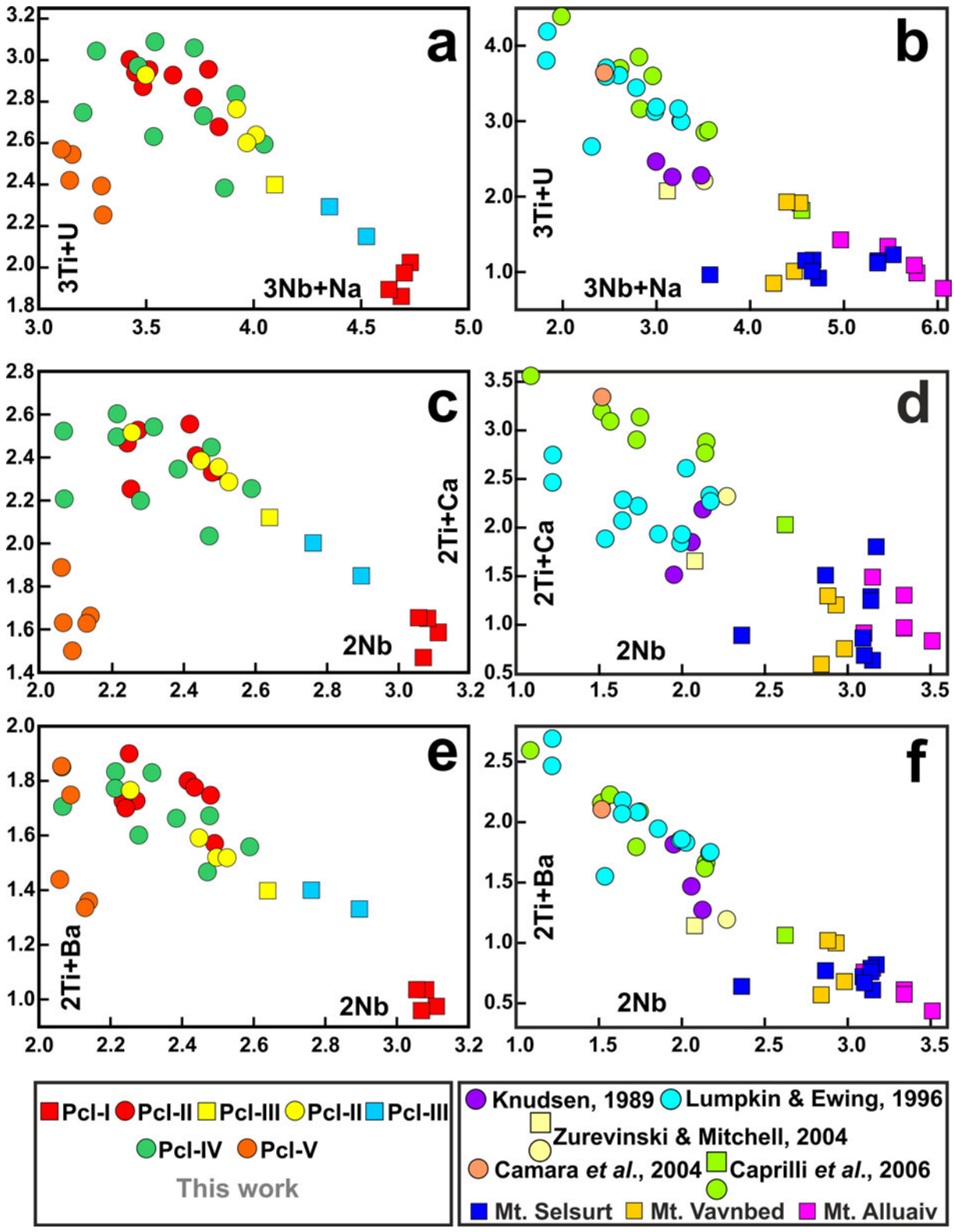

Fig. 7. Different substitutional mechanisms for pyrochlore-group minerals. (a) $3Nb^{5+}+Na^{+} \rightarrow 3Ti^{4+}+U^{4+}$ (apfu) substitution illustrating relative enrichment of Ti in the late generation pyrochlore (Pcl-II to Pcl-IV) from the Sevattur albitites in agreement with the global U-rich pyrochlore occurrences (b), showing a similar positive correlation. (c) $2Nb^{5+} \rightarrow 2Ti^{4+}+Ca^{2+}$ (apfu) substitution illustrating Ti and Ca enrichment in the late-generation pyrochlore (Pcl-II to Pcl-IV) from the Sevattur albitite. (d) Similar Ti and Ca enrichment is not evident for U-rich pyrochlore from other occurrences. (e) $2Nb^{5+} \rightarrow 2Ti^{4+}+Ba^{2+}$ (apfu) illustrating Ba enrichment in the late-generation pyrochlore (Pcl-II to Pcl-IV), especially in Pcl-V. (f) A strong positive correlation is also observed for other occurrences. Note that in all the bivariate plots, Pcl-V compositions are clustered and fall below the principal trend illustrating intense alteration relative to other pyrochlore (Pcl-I to Pcl-IV). The solid squares and corresponding solid circles of the same colour represent a core and rim compositional variation, respectively. Individual solid squares and circles represent either discrete or intermediate zone compositions. (Data source: Chakhmouradian and Mitchell, 2002 for Mt. Selsurt, Mt. Vavnbed and Mt. Alluaiv; given in the key: Knudsen, 1989, Lumpkin and Ewing, 1996, Zurevinski and Mitchell, 2004, Cámara *et al.*, 2004 and Caprilli *et al.*, 2006).

https://doi.org/10.1180/mgm.2021.6 Published online by Cambridge University Press

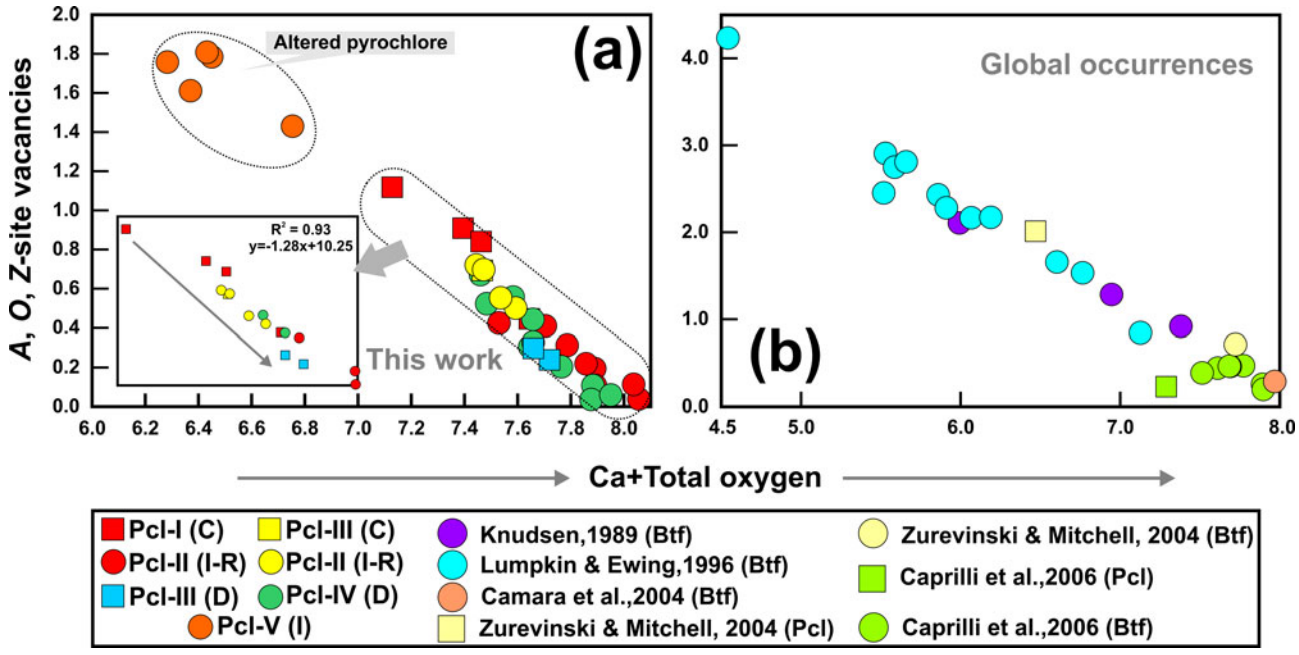

Fig. 8. (a) Substitution of *A*-, *O*- and *Z*-site vacancies by Ca and oxygens (total) (apfu) illustrating a strong negative trend for Pcl-I to Pcl-IV with an overall R^2 value of 0.93 for Pcl-I to Pcl-IV (*inset*). This explains the near stoichiometric compositions of Pcl-II to Pcl-IV. Note that the extensively altered pyrochlore are characterised by significant *A*, *O*, and *Z*-site vacancies. (b) A similar trend is observed for other occurrences of pyrochlore-group minerals, especially within betafite (Btf) group. (Data sources: Knudsen, 1989, Lumpkin and Ewing, 1996, Zurevinski and Mitchell, 2004, Cámara *et al*., 2004 and Caprilli *et al*., 2006).

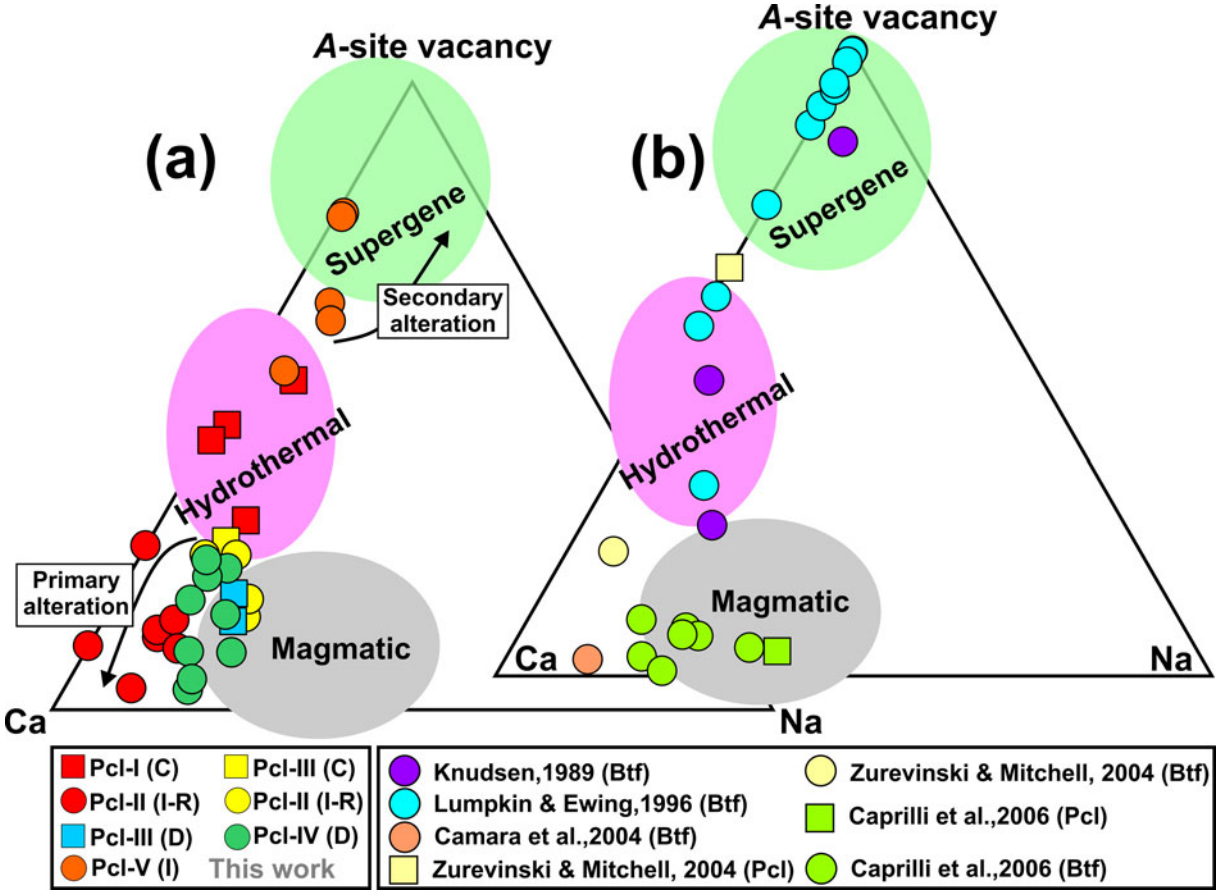

Fig. 9. (a) Compositional variation of the *A*-site cations (apfu) and lattice vacancies of pyrochlore group minerals from the Sevattur albitite (after Nasraoui and Bilal, 2000). Note that the core of Pcl-I plots within the hydrothermal field and subsequent pyrochlore generations (Pcl-II to Pcl-IV) plots towards the magmatic field, illustrating a strong Ca enrichment by primary alteration. Highly-altered and metamict pyrochlore (Pcl-IV) evolve towards the supergene field, demonstrating considerable *A*-site vacancies due to secondary alteration. (b) *A*-site compositional variation of pyrochlore from other occurrences. In common with the Sevattur, pyrochlore from the Oka carbonatite complex (Zurevinski and Mitchell, 2004) show a similar trend. (Data sources: Knudsen, 1989, Lumpkin and Ewing, 1996, Zurevinski and Mitchell, 2004, Cámara *et al*., 2004 and Caprilli *et al*., 2006).

https://doi.org/10.1180/mgm.2021.6 Published online by Cambridge University Press

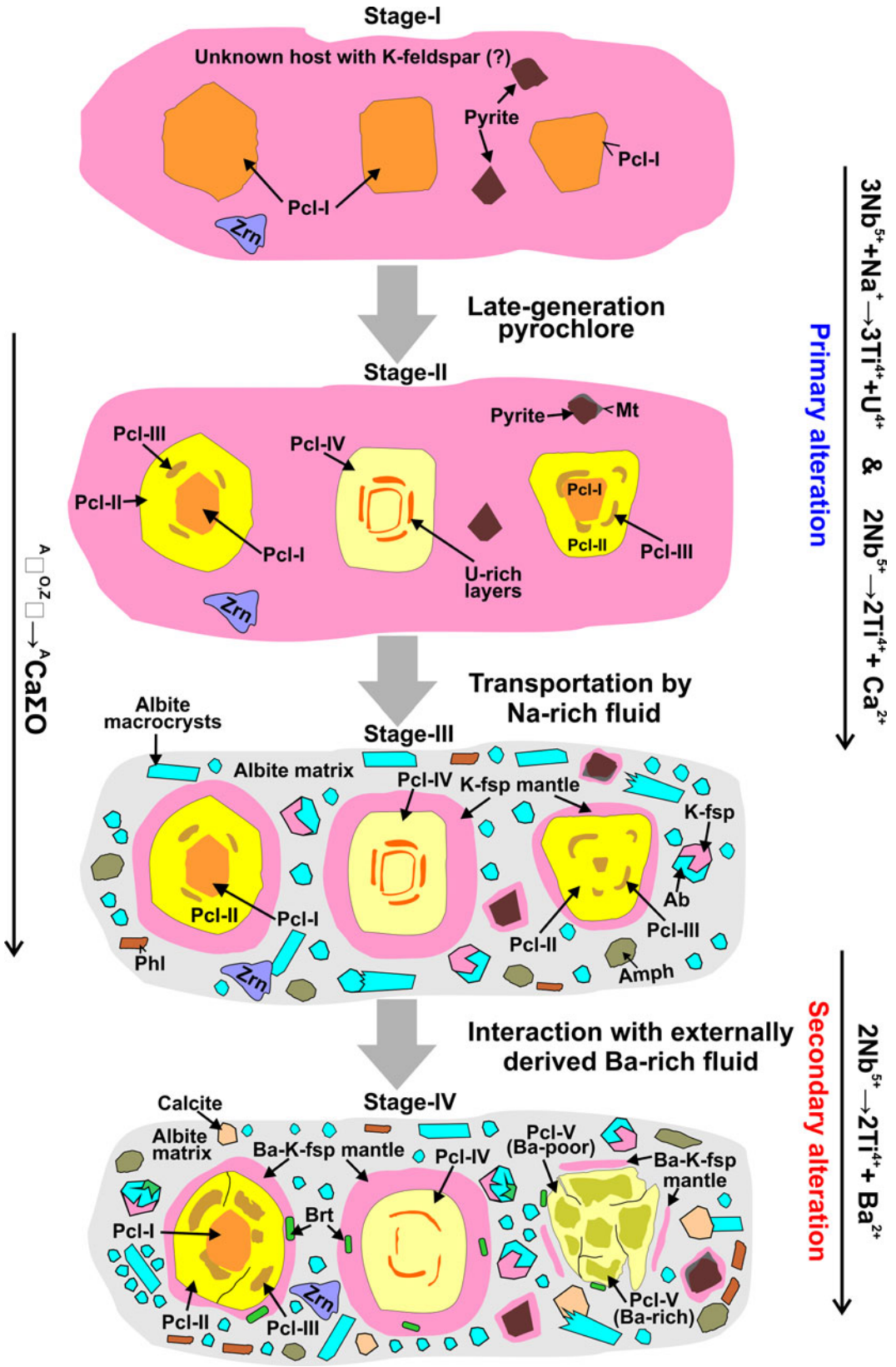

Fig. 10. Schematic diagram illustrating the generalised sequence of formation of the different pyrochlore types and associated minerals in Sevattur albitite. The initial stages (I and II) of pyrochlore formation is restricted to the unknown host and later carried to the current host (stage-III and -IV) as antecrysts. Note that the Ba-enrichment (stage-IV) mainly occurs in the albitite resulting in Pcl-V and baryte formation (see 'discussion' for further explanations).

https://doi.org/10.1180/mgm.2021.6 Published online by Cambridge University Press

and associated betafite from these complexes plot close to the magmatic field (Fig. 9b). At Oka, this trend is interpreted as a consequence of magma mixing, and the pyrochlore are essentially antecrysts, i.e. formed during successive pulses of carbonatite magma and finally carried by rheological processes into the magma which formed their current host rock. At Sevattur, this trend can be explained by the fact that the Pcl-I and the other pyrochlore were formed at different times, i.e. Pcl-I and Pcl-II to -IV are not related genetically, and their current juxtaposition is coincidental (stage-I and -II, Fig. 10) and similar to the magma mixing model proposed for Oka pyrochlore (Zurevinski and Mitchell, 2004; Chen and Simonetti, 2013). However, none of the Pcl-II to Pcl-IV are considered primary magmatic minerals, and probably formed from a U-rich hydrothermal fluid of unknown parentage which nucleated upon pre-existing Pcl-I (stage-II, Fig. 10). In this case, all the pyrochlore in Sevattur albitite can be considered as antecrysts.

Although albitites might be formed by the extensive sodic metasomatism of diverse protoliths ranging from the granite to nepheline syenites (Chakhmouradian and Mitchell; 2002; Chakrabarty *et al.*, 2016; 2018) other primary origins are possible. In carbonatite complexes, extreme sodic fenitisation is considered to produce albitites (Le Bas, 2008; Elliot *et al.* 2018). The lack of definitive field and petrographic evidence currently preclude the development of a model for the genesis of the Sevattur albitite veins. However, the field observations suggest that the albitite veins are formed from a Na-rich hydrothermal fluid of unknown parentage. This hydrothermal fluid apparently also carried pyrochlore (Pcl-I to Pcl-IV) as antecrysts together with K-feldspar matrix material (stage-III, Fig. 10). This K-feldspar matrix material upon interaction with a Ba-rich fluid forms Ba-rich potassium feldspar mantles around the pyrochlore. Furthermore, partial disruption of this mantle led to the replacement of Ca by Ba forming Ba-rich pyrochlore (Pcl-V). This is in agreement with the ubiquitous presence of baryte with Pcl-V (stage-IV, Fig. 10). In contrast to the albitites, significant U mobility took place in the calcite and dolomite carbonatite-hosted U-rich pyrochlore which lacks feldspar mantles.

Conclusions

Pyrochlore of the Sevattur albitite are unusual in terms of their texture and composition, being exceptionally U-rich. The characteristic textural feature of the Sevattur albitite is the presence of thick orbicular mantles of Ba-rich potassium feldspar upon pyrochlore and other minerals. On the basis of texture and composition, five different pyrochlore types (Pcl-I to Pcl-V) are recognised. Pcl-I are present exclusively as relict cores in association with Pcl-II and -III. In contrast, the later-generations of pyrochlore (Pcl-II to Pcl-IV) are either present as discrete grains or in combinations with each other. The early pyrochlore (Pcl-I) are Nb-, U-rich and Ca-, Ti-poor compared to the later pyrochlore (Pcl-II to Pcl-IV). The Ca and Ti enrichment in Pcl-II to Pcl-IV is considered as primary with two major substitutions: $3Nb^{5+} + Na^{+} \rightarrow 3Ti^{4+} + U^{4+}$ and $2Nb^{5+} \rightarrow 2Ti^{4+} + Ca^{2+}$, respectively (Fig. 10). A further stage of alteration is related to the Ba-enrichment in all the pyrochlore by the $2Nb^{5+} \rightarrow 2Ti^{4+} + Ba^{2+}$ substitution and here considered as secondary alteration leading to the patchy zoning in Pcl-II to -IV (Fig. 10). This substitution and extensive metamictisation produce Ba-enrichment in Pcl-V as the orbicular mantle around Pcl-V is partially broken (Fig. 10). This signifies that the orbicular mantling in Pcl-I to Pcl-IV acted as a protective shield inhibiting metamictisation and uranium loss during the primary and secondary alteration processes.

The compositional variations, particularly Ca–Na–*A*-site vacancies, suggest that Pcl-I are hydrothermal and are not related genetically to the other pyrochlore types. In comparison, Pcl-II to Pcl-IV were formed late in the paragenetic sequence nucleating on Pcl-I. Such compositionally diverse pyrochlore associations indicate that these are antecrysts, and this assemblage represents the rheological mixing process in the albitite host.

Acknowledgements. This work is supported by the Ministry of Mines (MOM), India through an Extra Mural Project (F.No. 8/4/2009-Met.IV Dt. 27.11.2014) awarded to AKS and AC. MD, SB, and AC also acknowledge Prof. K. N. Ganesh, Director, IISER Tirupati for providing financial assistance through an Institute Travel Grant to carry out necessary field work. R. H. Mitchell's work on alkaline rocks is supported by the Natural Sciences and Engineering Research Council of Canada, Lakehead University and Almaz Petrology Inc. We acknowledge the help rendered by Mr. S. Kartihikeyan for granting us the access into the vermiculite quarry at Sevattur to collect the albitite samples for this study. We acknowledge Pritam Saha and Priyadarshan Singha for their support during the field work. Victor V. Sharygin, Anton R. Chakhmouradian, Anatoly N. Zaitsev, and an anonymous reviewer are thanked for comments on this manuscript. We acknowledge Stuart Mills and Helen Kerbey for the Editorial and Production aspects of the publication of this work.

References

Ackerman L., Magna T., Rapprich, V., Upadhyay D., Krátký O., Čejková B., Erban V., Kochergina Y.V. and Hrstka T. (2017) Contrasting petrogenesis of spatially related carbonatites from Samalpatti and Sevattur, Tamil Nadu, India. *Lithos*, **284**, 257–275.

Andersen T. (1986) Magmatic fluids in the Fen carbonatite complex, SE Norway. *Contributions to Mineralogy and Petrology*, **93**, 491–503.

Atencio D., Andrade M.B., Christy A.G., Gieré R. and Kartashov P.M. (2010) The pyrochlore supergroup of minerals: nomenclature. *The Canadian Mineralogist*, **48**, 673–698.

Bhushan S.K. (2015) Geology of the Kamthai rare earth deposit. *Journal of the Geological Society of India*, **85**, 537–546.

Bhushan S.K. and Kumar A. (2013) First carbonatite hosted REE deposit from India. *Journal of the Geological Society of India*, **81**, 41–60.

Bonazzi P., Bindi L., Zoppi M., Capitani G.C. and Olmi F. (2006) Single-crystal diffraction and transmission electron microscopy studies of "silicified" pyrochlore from Narssârssuk, Julianehaab district, Greenland. *American Mineralogist*, **91**, 794–801.

Borodin L.S., Gopal V., Moralev V.M., Subramanian V. and Ponikarov V. (1971) Precambrian carbonatites of Tamil Nadu, South India. *Journal of the Geological Society of India*, **12**, 101–112.

Bosi F., Biagioni C. and Oberti R. (2019) On the chemical identification and classification of minerals. *Minerals*, **9**, 591.

Cámara F., Williams C.T., Ventura G.D., Oberti R. and Caprilli E. (2004) Non-metamict betafite from Le Carcarelle (Vico volcanic complex, Italy): occurrence and crystal structure. *Mineralogical Magazine*, **68**, 939–950.

Caprilli E., Della Ventura G., Williams T.C., Parodi G.C. and Tuccimei P. (2006) The crystal chemistry of non-metamict pyrochlore–group minerals from Latium, Italy. *The Canadian Mineralogist*, **44**, 1367–1378.

Chakhmouradian A.R. and Mitchell R.H. (2002) New data on pyrochlore- and perovskite-group minerals from the Lovozero alkaline complex, Russia. *European Journal of Mineralogy*, **14**, 821–836.

Chakhmouradian A.R., Reguir E.P., Kressall R.D., Crozier J., Pisiak L.K., Sidhu R. and Yang P. (2015) Carbonatite-hosted niobium deposit at Aley, northern British Columbia (Canada): Mineralogy, geochemistry and petrogenesis. *Ore Geology Reviews*, **64**, 642–666.

Chakrabarty A., Mitchell R.H., Ren M., Saha P.K., Pal S., Pruseth K.L. and Sen A.K. (2016) Magmatic, hydrothermal and subsolidus evolution of the agpaitic nepheline syenites of the Sushina Hill Complex, India: implications for

the metamorphism of peralkaline syenites. *Mineralogical Magazine*, **80**, 1161–1193.

Chakrabarty A., Mitchell R.H., Ren M., Pal S., Pal S. and Sen A.K. (2018) Nb–Zr–REE re-mobilization and implications for transitional agpaitic rock formation: insights from the Sushina Hill Complex, India. *Journal of Petrology*, **59**, 1899–1938.

Chebotarev D.A., Doroshkevich A., Klemd R. and Karmanov N. (2017) Evolution of Nb-mineralization in the Chuktukon carbonatite massif, Chadobets upland (Krasnoyarsk Territory, Russia). *Periodico di Mineralogia*, **86**, 99–118.

Chen W. and Simonetti A. (2013) In-situ determination of major and trace elements in calcite and apatite, and U–Pb ages of apatite from the Oka carbonatite complex: Insights into a complex crystallisation history. *Chemical Geology*, **353**, 151–172.

Christy A.G. and Atencio D. (2013) Clarification of status of species in the pyrochlore supergroup. *Mineralogical Magazine*, **77**, 13–20.

Chudy T.C. (2013) *The Petrogenesis of the Fir Carbonatite System, East-Central British Columbia, Canada*. PhD dissertation, University of British Columbia, Vancouver, Canada.

Dostal J. (2016) Rare metal deposits associated with alkaline/peralkaline igneous rocks. *Reviews in Economic Geology*, **18**, 33–54.

Droop G.T.R. (1987) A general equation for estimating Fe^{3+} concentrations in ferromagnesian silicates and oxides from microprobe analyses, using stoichiometric criteria. *Mineralogical Magazine*, **51**, 431–435.

Dumańska-Słowik M., Pieczka A., Tempesta G., Olejniczak Z. and Heflik W. (2014) "Silicified" pyrochlore from nepheline syenite (mariupolite) of the Mariupol Massif, SE Ukraine: A new insight into the role of silicon in the pyrochlore structure. *American Mineralogist*, **99**, 2008–2017.

Elliott H.A.L., Wall F., Chakhmouradian A.R., Siegfried P.R., Dahlgren S., Weatherley S., Finch A.A., Marks M.A.W., Dowman E. and Deady E. (2018) Fenites associated with carbonatite complexes: A review. *Ore Geology Reviews*, **93**, 38–59.

Essene E.J., Claflin C.L., Giorgetti G., Mata P.M., Peacor D.R., Arkai P. and Rathmell M.A. (2005) Two-, three- and four-feldspar assemblages with hyalophane and celsian: implications for phase equilibria in $BaAl_2Si_2O_8$–$CaAl_2Si_2O_8$–$NaAlSi_3O_8$–$KAlSi_3O_8$. *European Journal of Mineralogy*, **17**, 515–535.

Giebel R.J., Marks M.A., Gauert C.D. and Markl G. (2019) A model for the formation of carbonatite-phoscorite assemblages based on the compositional variations of mica and apatite from the Palabora Carbonatite Complex, South Africa. *Lithos*, **324**, 89–104.

Giovannini A.L., Mitchell R.H., Neto A.C.B., Moura C.A., Pereira V.P. and Porto C.G. (2020) Mineralogy and geochemistry of the Morro dos Seis Lagos siderite carbonatite, Amazonas, Brazil. *Lithos*, **360**, 105433.

Harris P.M. (1965) Pandaite from the Mrima Hill niobium deposit (Kenya). *Mineralogical Magazine*, **35**, 277–290.

Hatert F. and Burke E.A. (2008) The IMA–CNMNC dominant-constituent rule revisited and extended. *The Canadian Mineralogist*, **46**, 717–728.

Hawthorne F.C., Oberti R., Harlow G.E., Maresch W.V., Martin R.F., Schumacher J.C. and Welch M.D. (2012) Nomenclature of the amphibole supergroup. *American Mineralogist*, **97**, 2031–2048.

Hogarth D.D. (1977) Classification and nomenclature of the pyrochlore group. *American Mineralogist*, **62**, 403–410.

Hogarth D.D., Williams C.T. and Jones P. (2000) Primary zoning in pyrochlore group minerals from carbonatites. *Mineralogical Magazine*, **64**, 683–697.

Jäger E., Niggli E. and Van der Veen A.H. (1959) A hydrated barium–strontium pyrochlore in a biotite rock from Panda Hill, Tanganyika 1. *Mineralogical Magazine*, **32**, 10–25.

Khromova E.A., Doroshkevich A.G., Sharygin V.V. and Izbrodin L.A. (2017) Compositional evolution of pyrochlore-group minerals in carbonatites of the Belaya Zima Pluton, Eastern Sayan. *Geology of Ore Deposits*, **59**, 752–764.

Knudsen C. (1989) Pyrochlore Group Minerals from the Qaqarssuk Carbonatite Complex. Pp. 80–99 in: Lanthanides, Tantalum and Niobium (P. Möller, Petr Ćerný and Francis Saupé editors). Springer Verlag, Berlin.

Krishnamurthy P. (1977) On some geochemical aspects of the Sevattur carbonatite complex, North Arcot District, Tamil Nadu. *Journal of the Geological Society of India*, **18**, 265–274.

Krishnamurthy P. (2019) Carbonatites of India. *Journal of the Geological Society of India*, **94**, 117–138.

Le Bas M.J. (2008) Fenites associated with carbonatites. *The Canadian Mineralogist*, **46**, 915–932.

Lee M.J., Lee J. I., Garcia D., Moutte J., Williams C.T., Wall F. and Kim Y. (2006) Pyrochlore chemistry from the Sokli phoscorite–carbonatite complex, Finland: implications for the genesis of phoscorite and carbonatite association. *Geochemical Journal*, **40**, 1–13.

Linnen R.L. and Cuney M. (2005) Granite–related rare–element deposits and experimental constraints on Ta–Nb–W–Sn–Zr–Hf mineralisation, in Linnen RL and Samson IM, eds., rare-element geochemistry and mineral deposits. Pp. 45–68 in: *Rare-Element Geochemistry and Mineral Deposits, Vol. 17* (R.L. Linnen and I.M. Samson, editors). Geological Association of Canada.

Linnen R.L., Samson I.M., Williams-Jones A.E. and Chakhmouradian A.R. (2014) 13.21 – Geochemistry of the rare-earth element, Nb, Ta, Hf, and Zr Deposits. *Treatise on Geochemistry*, **13**, 543–568.

Lumpkin G.R. and Ewing R.C. (1995) Geochemical alteration of pyrochlore group minerals: pyrochlore subgroup. *American Mineralogist*, **80**, 732–743.

Lumpkin G.R. and Ewing R.C. (1996) Geochemical alteration of pyrochlore group minerals: Betafite subgroup. *American Mineralogist*, **81**, 1237–1248.

Mackay D.A.R. and Simandl G.J. (2014) Geology, market and supply chain of niobium and tantalum — a review. *Mineralium Deposita*, **49**, 1025–1047.

Melgarejo J.C., Costanzo A., Bambi A.C., Gonçalves A.O. and Neto A.B. (2012) Subsolidus processes as a key factor on the distribution of Nb species in plutonic carbonatites: The Tchivira case, Angola. *Lithos*, **152**, 187–201.

Mitchell R.H. (2015) Primary and secondary niobium mineral deposits associated with carbonatites. *Ore Geology Reviews*, **64**, 626–641.

Mitchell R.H. and Kjarsgaard B.A. (2002) Solubility of niobium in the system $CaCO_3$–$Ca(OH)_2$–$NaNbO_3$ at 0.1 GPa pressure. *Contributions to Mineralogy and Petrology*, **144**, 93–97.

Mitchell R.H. and Kjarsgaard B.A. (2004) Solubility of niobium in the system $CaCO_3$–CaF_2–$NaNbO_3$ at 0.1 GPa pressure: implications for the crystallisation of pyrochlore from carbonatite magma. *Contributions to Mineralogy and Petrology*, **148**, 281–287.

Mitchell R.H. and Smith D.L. (2017) Geology and mineralogy of the Ashram Zone carbonatite, Eldor Complex, Québec. *Ore Geology Reviews*, **86**, 784–806.

Mitchell R., Chudy T., McFarlane C.R. and Wu F.Y. (2017) Trace element and isotopic composition of apatite in carbonatites from the Blue River area (British Columbia, Canada) and mineralogy of associated silicate rocks. *Lithos*, **286**, 75–91.

Mitchell R.H., Wahl R. and Cohen A. (2020) Mineralogy and genesis of pyrochlore apatitite from The Good Hope Carbonatite, Ontario: A potential niobium deposit. *Mineralogical Magazine*, **84**, 81–91.

Nasraoui M. and Bilal E. (2000) Pyrochlores from the Lueshe carbonatite complex (Democratic Republic of Congo): a geochemical record of different alteration stages. *Journal of Asian Earth Sciences*, **18**, 237–251.

Naushad Md., Murthy P.V.R. and Cakhra M. (2019) Barium-rich alkali feldspar in basanite from central Kachchh, north-western India. *Current Science*, **116**, 1637.

Nickel E.H. (1992) Solid solutions in mineral nomenclature. *Mineralogy and Petrology*, **46**, 49–53.

Nickel E.H. and Grice J.D. (1998) The IMA Commission on New Minerals and Mineral Names: procedures and guidelines on mineral nomenclature. *Mineralogy and Petrology*, **64**, 237–263.

Palmer D.A. and Williams-Jones A.E. (1996) Genesis of the carbonatite-hosted fluorite deposit at Amba Dongar, India; evidence from fluid inclusions, stability isotopes, and whole rock–mineral geochemistry. *Economic Geology*, **91**, 934–950.

Paul D., Chandra J. and Halder M. (2020) Proterozoic Alkaline rocks and Carbonatites of Peninsular India: A review. *Episodes Journal of International Geoscience*, **43**, 249–277.

Pouchou J.L. and Pichoir F. (1991) Quantitative analysis of homogeneous or stratified microvolumes applying the model "PAP". Pp. 31–75 in: *Electron probe quantitation* (K.F.J. Heinrich and D.E. Newbury, editors). Plenum Press, New York.

https://doi.org/10.1180/mgm.2021.6 Published online by Cambridge University Press

Pressacco R. (2001) Geology of the Cargill Township residual carbonatite-associated phosphate deposit, Kapuskasing, Ontario. *Exploration and Mining Geology*, **10**, 77–84.

Pršek J., Ondrejka M., Bačík P., Budzyń B. and Uher P. (2010) Metamorphic-hydrothermal REE minerals in the Bacúch magnetite deposit, Western Carpathians, Slovakia:(Sr, S)-rich monazite-(Ce) and Nd-dominant hingganite. *The Canadian Mineralogist*, **48**, 81–94.

Raith M.M., Devaraju T.C. and Spiering B. (2014) Paragenesis and chemical characteristics of the celsian – hyalophane – K-feldspar series and associated Ba–Cr micas in baryte-bearing strata of the Mesoarchaean Ghattihosahalli Belt, Western Dharwar Craton, South India. *Mineralogy and Petrology*, **108**, 153–176.

Ramasamy R., Gwalani L.G. and Subramanian S.P. (2001) A note on the occurrence and formation of magnetite in the carbonatites of Sevvattur, North Arcot district, Tamil Nadu, Southern India. *Journal of Asian Earth Sciences*, **19**, 297–304.

Randive K. and Meshram T. (2020) An Overview of the Carbonatites from the Indian Subcontinent. *Open Geosciences*, **12**, 85–116.

Rukhlov A.S. and Bell K. (2010) Geochronology of carbonatites from the Canadian and Baltic Shields, and the Canadian Cordillera: clues to mantle evolution. *Mineralogy and Petrology*, **98**, 11–54.

Schleicher H., Todt W., Viladkar S.G. and Schmidt F. (1997) Pb/Pb age determinations on the Newania and Sevattur carbonatites of India: evidence for multi-stage histories. *Chemical Geology*, **140**, 261–273.

Schleicher H., Kramm U., Pernicka E., Schidlowski M., Schmidt F., Subramanian V., Todt W. and Viladkar S.G. (1998) Enriched subcontinental upper mantle beneath southern India: evidence from Pb, Nd, Sr, and C–O isotopic studies on Tamil Nadu carbonatites. *Journal of Petrology*, **39**, 1765–1785.

Schleicher H. (2019) In-situ determination of trace element and REE partitioning in a natural apatite–carbonatite melt system using synchrotron XRF microprobe analysis. *Journal of the Geological Society of India*, **93**, 305–312.

Sharygin V.V., Sobolev N.V. and Channer D.M.D. (2009) Oscillatory-zoned crystals of pyrochlore-group minerals from the Guaniamo kimberlites, Venezuela. *Lithos*, **112**, 976–985.

Starikova A.E., Bazarova E.P., Savel'eva V.B., Sklyarov E.V., Khromova E.A. and Kanakin S.V. (2019) Pyrochlore-group minerals in the granite-hosted Katugin rare-metal deposit, Transbaikalia, Russia. *Minerals*, **9**, 490.

Subramaniam V., Viladkar S.G. and Upendran R. (1978) Carbonatite alkali complex of Samalpatti, Dharmapuri district, Tamil Nadu. *Journal of the Geological Society of India*, **19**, 206–216.

Traversa G., Gomes C.B., Brotzu P., Buraglini N., Morbidelli L., Principato M.S., Ronca S. and Ruberti E. (2001) Petrography and mineral chemistry of carbonatites and mica-rich rocks from the Araxá complex (Alto Paranaíba Province, Brazil). *Anais da Academia Brasileira de Ciências*, **73**, 71–98.

Udas G.R. and Krishnamurthy P. (1970) Carbonatites of Sevathur and Jokipatti, Madras State, India, *Proceedings of Indian National Science Academy*, **36**, 331–343.

Uher P., Černy P., Chapman R., Hatar J. and Miko O. (1998) Evolution of Nb, Ta–oxide minerals in the Prašivá granitic pegmatites, Slovakia. II. External hydrothermal Pb, Sb overprint. *The Canadian Mineralogist*, **36**, 535–545.

Verplanck P.L., Mariano A.N. and Mariano A. (2016) Rare earth element ore geology of carbonatites. *Reviews in Economic Geology*, **18**, 5–32.

Viladkar S.G. and Bismayer U. (2014) U-rich pyrochlore from Sevathur carbonatites, Tamil Nadu. *Journal of the Geological Society of India*, **83**, 175–182.

Viladkar S.G. and Subramanian V. (1995) Mineralogy and geochemistry of the carbonatites of the Sevathur and Samalpatti complexes, Tamil–Nadu. *Journal of the Geological Society of India*, **45**, 505–517.

Walter B.F., Parsapoor A., Braunger S., Marks M.A.W., Wenzel T., Martin M. and Markl G. (2018) Pyrochlore as a monitor for magmatic and hydrothermal processes in carbonatites from the Kaiserstuhl volcanic complex (SW Germany). *Chemical Geology*, **498**, 1–16.

Williams C.T., Wall F., Woolley A.R. and Phillipo S. (1997) Compositional variation in pyrochlore from the Bingo carbonatite, Zaire. *Journal of African Earth Sciences*, **25**, 137–145.

Zaitsev A.N., Williams C.T., Wall, F. and Zolotarev A.A. (2012) Evolution of chemical composition of pyrochlore group minerals from phoscorites and carbonatites of the Khibina alkaline massif. *Geology of Ore Deposits*, **54**, 503–515.

Zhang M., Suddaby P., Thompson R.N. and Dungan M.A. (1993) The origins of contrasting zoning patterns in hyalophane from olivine leucitites, Northeast China. *Mineralogical Magazine*, **57**, 565–573.

Zurevinski S.E. and Mitchell R.H. (2004) Extreme compositional variation of pyrochlore-group minerals at the Oka carbonatite complex, Quebec: evidence of magma mixing? *The Canadian Mineralogist*, **42**, 1159–1168.

https://doi.org/10.1180/mgm.2021.6 Published online by Cambridge University Press